IOP Publishing Phys. Scr. 99 (2024) 075315 https://doi.org/10.1088/1402-4896/ad5887

Physica Scripta

RECEIVED
16 April 2024

REVISED
25 May 2024

ACCEPTED FOR PUBLICATION
14 June 2024

PUBLISHED
25 June 2024

PAPER

Enhancing connectivity/mobility in WBAN applications through detachable wearable multi-band MIMO antenna

Tale Saeidi[1,2,*], **Sahar Saleh**[1], **Nick Timmons**[1], **Saeid Karamzadeh**[3,4], **Ahmed Jamal Abdullah Al-Gburi**[5] and **Faroq Razzaz**[6,7]

[1] WiSAR Lab, Atlantic Technological University (ATU), Letterkenny, Co. Donegal F92 FC93, Ireland
[2] Electrical and Electronics Engineering Department, Faculty of Engineering and Natural, Sciences, İstinye University, Istanbul, Turkey
[3] Millimeter Wave Technologies, Intelligent Wireless System, Silicon Austria Labs, Linz, Austria
[4] Electrical and Electronics Engineering, Department, Faculty of Engineering and Natural Sciences, Bahçeşehir University, Istanbul, Turkey
[5] Microwave Research Group (MRG), Centre for Telecommunication Research & Innovation (CeTRI), Fakulti Kejuruteraan Elektronik dan Kejuruteraan Komputer (FKEKK), Universiti Teknikal Malaysia Melaka (UTeM), Hang Tuah Jaya, Durian Tunggal 76100, Malaysia
[6] Electrical Engineering Department, College of Engineering, Prince Sattam Bin Abdulaziz University, Al-Kharj 16278, Saudi Arabia
[7] Faculty of Engineering and Information Technology, Taiz University, Taiz, 6803, Yemen
[*] Author to whom any correspondence should be addressed.

E-mail: talecommunication@gmail.com and Tale.Saeidi@atu.i.e

Keywords: 5G, sub-6 GHz, spiral button antenna, wearable leaky wave antenna, multi-band antenna, WBAN

Abstract

The connectivity and mobility of a miniaturized multi-band four-port textile leaky wave multiple-input multiple-output (MIMO) antenna designed on a layer of denim ($\varepsilon_r = 1.6$, $\tan\delta = 0.006$) is enhanced by integrating it with two detachable spiral buttons designed on circular PTFE substrate ($\varepsilon_r = 2.1$, $\tan\delta = 0.001$). The connectivity and mobility enhancement of the proposed antenna is evaluated in terms of radiation and diversity parameters. Nested hexagonal split rings behind the buttons, U-shaped slots on textiles, a comb-shaped neutralization network, and an aperture-coupled feed technique are utilized. The unique structure of the buttons on a rigid substrate and the leaky wave antenna on the textile and their integration, the periodic nested elliptical and circular split ring resonators (CSRRs) slots on the aperture coupled to ground, are to expand the connectivity and mobility of the proposed MIMO antenna by offering multiple bands, higher isolation, broadside radiation, and low specific absorption rate (SAR). The leaky wave and button antennas have dimensions of $40 \times 30 \times 1$ mm^3 and a diameter of only 13 mm, respectively. The operational bands are 0.86–2.75 GHz, 2.9–4.85 GHz, 5.75–6.15 GHz, and 8–9.85 GHz, covering the L, C, S, and X bands. Additionally, diversity performance is evaluated by defining the envelope correlation coefficient (ECC), diversity gain (DG), Channel Capacity Loss (CCL), and mean effective gain (MEG). The simulation and measurement findings are in good agreement. Following that, it offers a maximum gain of 8.25 dBi, low SAR (<0.05), an ECC below 0.05, DG above 9.85 dB, CCL$<$ 0.25 bits/s/Hz, MEG <-3 dB, Circular polarization (CP), and strong isolation (>22 dB) between every two ports. These features make the proposed antenna an ideal option for MIMO communications and suitable for wireless local area network (WLAN) and fifth-generation (5G) communications.

1. Introduction

Wireless communications leverage multiple-input multiple-output (MIMO) technology for speed and reliability, using multiple antennas at both ends. They should have polarization diversity, which reduces spatial constraints and mitigates multipath fading. Therefore, techniques like defected ground structure (DGS), split ring resonators (SRRs), and electromagnetic band gaps (EBG) maintain performance in MIMO systems. Wireless Body Area Networks (WBANs), crucial for tracking, identity systems, and healthcare, demand flexible materials. However, they face signal disruptions due to movement, necessitating diverse setups such as combining the abovementioned techniques. Hence, compact wearable MIMO systems that benefit from vertical polarization can offer promising outcomes but pose setup challenges. Moreover, multi-band antennas are essential for accommodating various communication standards. This aids in on-body propagation in WBANs because the movement might cancel or shift some parts of the working bands. Hence, wearable systems require physical elasticity, robustness, and connectivity during motion [1–3]. To face the above challenges in wearable antennas, researchers have investigated various types of materials and antennas, such as conductive textile antennas [4], elastic substrate-based antennas [5], and button-like antennas [6]. Most of the on-body antennas are solely made on textile substrates. However, the body's textiles can bend and stretch, thereby altering the resonance frequency, bandwidth, and radiation efficiency of textile antennas. To overcome this issue, garment components such as buttons were incorporated instead of fully textile substrates [7–9]. Button antennas are resilient to folding and flexing, are rarely susceptible to deformation, temperature fluctuations, and moisture, and can be easily connected to textiles using conventional sewing techniques. Furthermore, the spacing between button antennas and human tissues reduces the low specific absorption rate (SAR). Several button antennas have been studied for wearables applications [10]. Unfortunately, polarization diversity has not been achieved in these antennas.

Apart from the challenges that wearable antennas face and mentioned before, having high data rate transition, circular/ dual polarization, multipath fading, and path loss should also be considered. Therefore, a MIMO antenna designed on a textile utilizing garment components such as zippers and buttons will be promising to fulfill most requirements for a highly diverse wearable MIMO antenna. A four-port high-performance leaky wave wearable MIMO antenna can enhance connectivity and mobility with its advanced MIMO capabilities and dynamic beam steering. These features ensure higher data rates, improved signal quality, and reliable performance in mobile applications. It maintains robust connections with multiple base stations, ensuring seamless handover and uninterrupted connectivity as the user moves. This is crucial for sports, healthcare, military, and everyday applications. Additionally, MIMO systems filter out interference, focusing on the desired signal. Integrating a four-port MIMO textile antenna and a detachable button allows seamless antenna integration into the fabric, easy connection and disconnection, and resistance to degradation caused by folding. Antennas must support various communication standards while providing dual-polarization, pattern diversity, and miniaturization. These features enhance internet connections, eliminate polarization inconsistencies, and improve robustness and receptivity. Moreover, by establishing direct contact between the receiver and transmitter, a higher signal-to-noise ratio (SNR) can be achieved, along with improved power balancing between vertical and horizontal polarization. Circular polarization (CP) enabled this possibility by authors in [11]. Affordable and viable alternatives, such as low-cost, high RF efficiency, and circularly polarized antennas, were proposed. However, they could only operate in a single frequency range, limiting their applications, and pattern diversity was not achieved [12, 13]. According to the authors, achieving all these requirements simultaneously in a wearable button antenna has not been accomplished. Even those presented in [11–13] overlooked most of these requirements. Hence, a circularly polarized or polarization-diverse (dual or triple polarization) multi-band textile MIMO antenna incorporating a button can be employed to face most of these issues.

Several MIMO antennas with three and four ports designed on wearable and rigid substrates are investigated to present state-of-the-art MIMO antennas. Later in the paper, their performance will be compared with our proposed antenna.

A disk-shaped compact three-port planar MIMO antenna was proposed and fabricated for the 2.4 GHz WLAN band with a radius of 16 mm. The antenna was compact and showed a high isolation of 24 dB. However, it only covered a single band and offered a deficient gain of 2.3 dBi. Besides, this button-like antenna was designed on a rigid substrate such as FR4, and no diversity investigation of the MIMO antenna was carried out [14]. Another 3-port MIMO with a dimension of 260×200 m^2 was designed on a FR4 for LTE, WLAN, and 5G C-band. The antenna could only obtain a maximum gain of 5 dBi and an ECC of less than 0.1, having a large dimension [15]. [16] designed a 3 port MIMO only on a rigid substrate operating at multi modes with dimensions of 28.6 mm^2, maximum gain of 7 dBi, ECC of less than 0.08, and maximum efficiency of less than 70%. However, not most of the diversity parameters of the MIMO antenna were investigated. Another three-port MIMO antenna used FR4 to design a circulary polarized (CP) antenna at 5.2 GHz with high isolation of more than 20 dB. Furthermore, the antenna could offer CCL of less than 0.1, acceptable total active reflection coefficient, and a maximum gain of 4.2 dBi with a dimension of 65×45 mm^2. But, still, it was bulky with low gain on only a rigid substrate [17]. Last but not least, a three-terminal ultra-wideband (UWB) MIMO was designed on a textile substrate. The antenna covered the frequency range from 2.74 to 12.33 GHz (about 127.27%) with a port isolation of >26 dB over the entire UWB frequency range. The ECC was <0.025 with a high-diversity gain (DG>9.9 dB) throughout the operating band. The channel capacity loss for the proposed MIMO antenna was<0.13 bit/s/Hz. The imprinted optimized UWB MIMO antenna captured a 55×35 mm^2

area. It also offered a maximum gain of 6.9 dBi. The antenna used only a layer of jeans, which can be susceptible to bending. Besides, the antenna's performance was not examined with different degrees of bending [18].

After presenting the state of the art for MIMO antenna with 3 ports, the most recent MIMO antennas with 4 ports are considered to be compared with the proposed antenna later on. [19] introduced a versatile, flat, slim, ultra-wideband textile antenna featuring four tree-shaped elements. The antenna's frequency range extended from 3.18 to 4.60 GHz and 8.89 to 12 GHz, exhibiting notch characteristics across the entire WLAN spectrum (2.4–2.485 GHz, 5.15–5.85 GHz), C-band uplink (5.925–6.425 GHz), GEOSAT LNB (7.25–7.75 GHz), and ITU (7.75–8.5 GHz) application bands. Furthermore, it demonstrated satisfactory isolation of approximately 20.5 dB between ports. Additionally, it achieved a maximum gain of less than 6 dBi, a Channel Capacity Loss (CCL) of less than 0.7 bits/s/Hz, and an ECC of less than 0.2, all within a size of 40 mm^2. Despite its commendable performance across multiple bands, it was only designed on a textile substrate prone to movement and not a full-body voxel used for SAR investigation. Another MIMO antenna with four ports had overall dimensions of 54 mm $\times$ 54 mm $\times$ 0.13 mm. This antenna obtained a peak gain of 5 dB, featuring semi-omnidirectional and bidirectional patterns in both planes. The DG remained at or above 9.9 dB throughout its operational frequency band. The ECC was maintained below 0.03 from 3.5 GHz to 4 GHz and below 0.01 from 4 GHz to 11 GHz. The CCL was also kept at or below 0.5 bit s^{-1} Hz^{-1} [20]. However, it had relatively large dimensions, was fabricated only on a layer of flexible, rigid substrate that was not wearable, and no SAR evaluation was performed. A flexible MIMO antenna was proposed for applications in Sub-6 GHz 5G and X-band frequencies, featuring four ports and four interconnected elements. The compact structure occupied a low profile of 54.97 mm^2. Demonstrating impressive performance, the flexible antenna achieved a minimum efficiency of 70% and a maximum gain of 4 dBi. It also delivered a bandwidth spanning from 3.34 GHz to 5.01 GHz (40%) and 8.9 GHz to 9.2 GHz (3.31%). It met MIMO diversity requirements with an ECC below 0.17. Nevertheless, most of the MIMO diversity factors were not investigated, and the antenna obtained lower efficiency and gain with a larger size [21]. A compact wearable antenna system employing multiple-input multiple-output (MIMO) technology was proposed for applications in the new radio band 79 (4.4–5 GHz). This system comprised four coplanar waveguide-fed antennas, each designed as an identical hexagonal-shaped monopole radiator printed on a polyimide substrate measuring 88.7 $\times$ 68.7 mm^2. With an emphasis on enhanced isolation, the antenna achieved isolation levels exceeding 17 dB while exhibiting a peak gain ranging from approximately 3.8 to 4 dBi across the operating frequency range. Moreover, the antenna demonstrated a radiation efficiency ranging from 88% to 90%. A flexible substrate enabled the antenna to conform to different shapes, a feature validated through bending analysis. Apart from all those evaluations, the antenna gain was too small with large dimensions [22]. The antenna was designed to operate in the UWB spectrum (3.1–12 GHz) with an impedance bandwidth of 8.9 GHz. The size of the unit cell and MIMO antenna are $0.25\lambda_0 \times 0.2\lambda_0 \times 0.015\lambda_0$ and $0.52\lambda_0 \times 0.52\lambda_0 \times 0.015\lambda_0$, respectively. The antenna had a maximum efficiency of 93% and a peak gain of 4.62 dBi. The investigation of diversity metrics was performed, and the results obtained were ECC < 0.08 and DG < 9.99 dB. The computed CCL and TARC values were $<$0.13 bits/s/Hz and <-12 dB, respectively. However, the antenna was designed on only the textile layer, and the gain was low with those large dimensions [23]. Using jeans textile material, a compact MIMO antenna with dual or quad elements was proposed for WiMAX and 5G applications. The wideband characteristics of a single-element antenna covering a frequency range from 2.74 to 4.41 GHz (47%) were analyzed. Excellent isolation exceeding 19 dB and maximum gain below 5 dBi were achieved across the entire application band with dimensions of 58 $\times$ 55 mm^2. Diversity parameters such as ECC (< 0.2), DG (> 9.6 dB), and mean effective gain (MEG $= \pm 0.3$ dB) were observed to fall within satisfactory ranges; but the gain was low and only a layer of textile was used [24]. All the presented MIMO antennas in [14–27] were designed on either only rigid or textile substrates. There were also low gains and efficiency, with relatively larger sizes than their operating frequency and covering only a single or two bands. Therefore, a polarization-diverse (dual or triple polarization) textile MIMO antenna incorporating a button can be employed to face most of these limitations.

Contribution of study:

Following the challenges and limitations that recent previous research presented in the previous paragraphs, this study proposes a unique wearable MIMO antenna structure that integrates two multi-band detachable spiral button antenna with a four-port wearable MIMO leaky wave antenna (LWA) that enables lower 5G band and sub-6 GHz communications (also covering L, C, S, and X bands) to enhance the connectivity, mobility, and compatibility of MIMO communications. The LWA was selected for this work due to its ability to perform beam steering and frequency scanning, which is suitable for body-centric and WBAN applications on the battlefield. Multi-band capability, compactness, and user comfort are enhanced by including metal and two detachable spiral buttons as a standard part of a garment. Unlike commonly used cloth parts such as zippers, these buttons are not significantly sensitive to bending and harsh environments. This approach aims to be more practical and replicate the same scenario as when genuine buttons available in the market are used. The antenna consists of a novel leaky-wave textile antenna (LWTA) with periodic coupled aperture slots on the ground and a comb-like

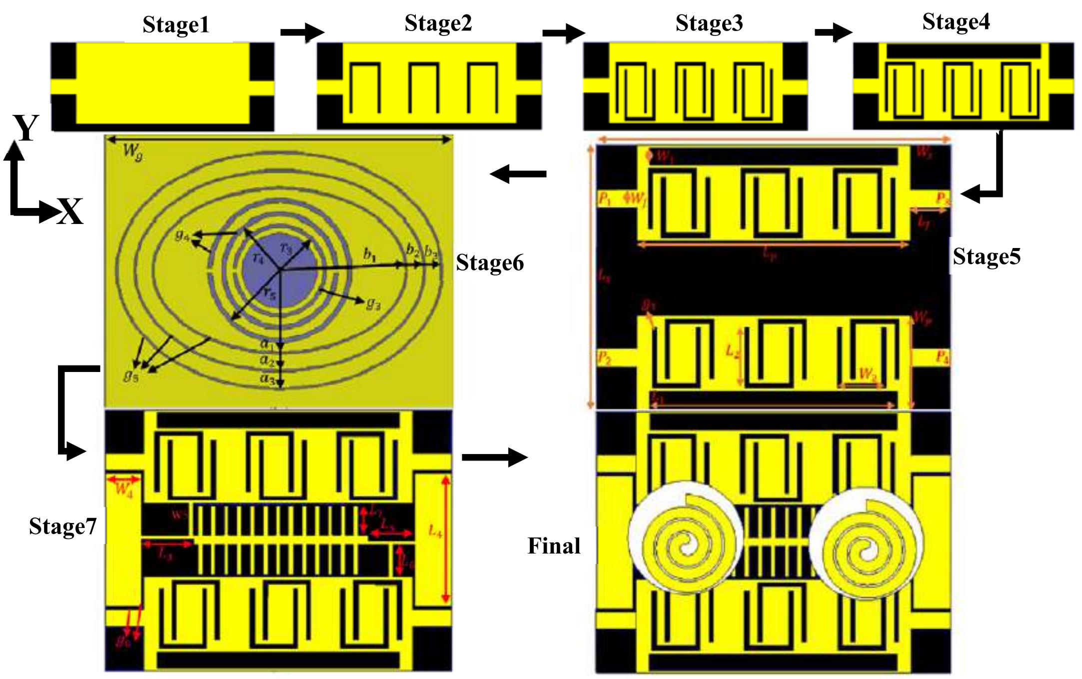

Figure 1. The design flowchart of the LWTA including each step of the design and the proposed prototype.

neutralization network (Later in the parametric study, the effects of the novel structure of the slots and their combination on miniaturization are presented). The aperture-coupled feed technique and the periodic slots on the ground miniaturize the overall dimensions of the antenna and facilitate the integration of the antenna with any possible electronic component in the future. Additionally, the particular structure of the LWTA and the nested U-shaped slots on the patch significantly assist in the miniaturization of the antenna based on its design frequency. The transversal and longitudinal tilt combination shifts the radiation pattern from a bi-directional pattern to a broadside pattern, suppressing the side and back lobes. Therefore, high gain, radiation efficiency, and high isolation are achieved after adding the comb-like network. The antenna can transmit a circular broadside radiation pattern and offer a monopole-like resonant mode. This monopole-like radiation pattern is utilized in the WiMAX and lower 5G spectrums for on-body data transfer. It also maintains an acceptable SAR level in all working bands, below the European standard's cut-off values.

After an informative introduction in section 1, section 2 focuses on evaluating and establishing the conceptual framework of the proposed multi-band button MIMO antenna, designed for WBAN applications and 5G communications. Section 3 thoroughly investigates the antenna's modeling and presents experimental results. Finally, section 4 concludes by summarizing the essential findings and providing recommendations.

2. Design process of the antenna

This section outlines the antenna configuration and design procedures. The MIMO LWTA is initially constructed for specific frequency bands before integrating the buttons. The radiation characteristics of the two-port configuration are examined and extended to a four-port setup. Incorporating the buttons enhances the performance. The comb-like neutralization network is employed to enhance isolation, impedance bandwidth, radiation efficiency, bandwidth, and gain while suppressing surface waves. The antenna mitigates backside radiation by combining transversal and longitudinal slots in U shapes, achieving a broadside radiation pattern. Integration of zippers and an LWTA yields constructive high broadside radiation characteristics. Current and electric-field concentrations were analyzed at various frequencies to elucidate antenna operation. Afterward, connectivity and mobility studies are conducted using nonuniform and measurement phantoms and actual human subjects, focusing on chest, arm, and shoulder regions for authentic conditions simulation. Critical parameters are optimized based on actual values obtained from principle equations before detailing the design process.

2.1. Design of Proposed MIMO LWTA without the Button Integration

Figure 1 illustrates various views of the proposed MIMO LWTA. Each design stage starts from two ports and progresses to four ports separately, and it is integrated with the neutralization networks later. In the next section,

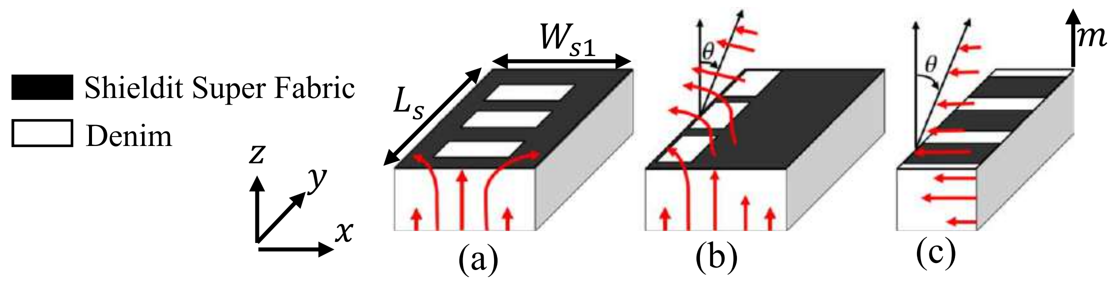

Figure 2. Asymmetry radiation principle: (a) TE_{10} mode in even structure, (b) leaky TE_{10} mode in uneven structure, and (c) leaky TE_{01} mode in even structure (θ is the approximated maximum angle of the radiation).

two spiral buttons are utilized to account for real-world scenarios. The effects on the human body will be discussed later in the results section of the article. The proposed LWTA incorporates a transmission line-fed rectangular area, with one end of the antenna serving as an excitation point and the other end terminated with a 50-ohm load (refer to figure 1, step 1). Initially, fundamental equations, as provided by [28], are employed to determine the dimensions of the rectangular patch and transmission line, enabling the antenna's design at 3.4 GHz (where $\lambda_0/2 < 44$ mm). However, these equations, being well-established principles, are not reiterated here. Subsequently, the design process for the proposed LWTA begins, adhering to the following rules, equations, and standards, which are essential for every LWA. It is worth noting that altering the length of an antenna can significantly affect its resonant frequency. Typically, an antenna's resonant frequency is inversely proportional to its length; as the antenna's length increases, its resonant frequency decreases, and vice versa. The principles of electromagnetic waves and the specific construction of the antenna govern this relationship. The design of the leaky wave structure prioritizes high directivity and gain, low loss, and structural simplicity. LWAs belong to a class of traveling-wave antennas characterized by a wave propagating along a long structure compared to the wavelength. They generate currents propagating along its longitudinal direction, resulting in end-fire and back-fire radiation patterns due to the open-stopband (OSB) phenomenon, as described in [29]. These antennas can be effectively modeled using balanced Composite right-/left-handed (CRLH) transmission lines, which combine the effects of capacitors and inductors. Enhancements are necessary to enable outward radiation from the body in a broadside direction.

The proposed LWTA incorporates asymmetric elements, including longitudinal slots aimed at improving the OSB and transverse slots designed to eliminate OSB issues, functioning like a series of left-handed capacitances (CL). Consequently, these elements modify the radiation pattern, making it more effective in the broadside direction rather than end-fire or back-fire. Moreover, these slots enhance isolation between antennas within the array and mitigate surface waves generated by LWAs. The characteristic mode method is employed to analyze and design these slots and evaluate their impact on the radiation pattern from the initial to the final stage of the design process, considering the principles of asymmetry radiation as depicted in figure 2 [30].

The periodic slots do not cover the entire substrate width (W_{s1}) and are positioned at an offset from one side (refer to figures 1 and 2). Additionally, the waveguide port must be excited with the TE_{10} mode, rather than the TE sub 01 mode, as in the dielectric inset. Following the proposed shape of the antenna and the improvement of the OSB issue through asymmetrical structure, the radiation mechanism of the new antenna is based on the asymmetry principle shown in figure 2. When the periodic slots are symmetrically located concerning the side walls, the vertically polarized TE_{10} mode does not induce any horizontal field in the antenna aperture, as depicted in figure 2(a). The transverse parts of the U-shaped slots in the proposed design utilize this principle. It implies that the electromagnetic waves emitted from the port exhibit polarizations perpendicular to the longitudinal planes of both the antenna and the transmission line. Considering the stub-loaded LWA, the parallel plates (the patch and ground layers) function as a filtering mechanism, allowing only the horizontal field to reach the waveguide aperture at the height of *m* from the dielectric interface in the space. Therefore, the symmetrical periodic structure renders the TE_{10} mode nonradiative when m is sufficiently high. The slots must be asymmetrically positioned to induce a potential difference in the parallel plates. This difference of potential generates a horizontally polarized TEM wave, which can propagate to the aperture and radiate into the free space region, as depicted in figure 2(b). The longitudinal parts of the U-shaped slots and the long slot next to them in the proposed design operate based on this principle. Thus, by adjusting the level of slot asymmetry, one can control the excitation level of this radiating horizontal wave, thereby altering the leakage rate of the TE_{10} leaky mode. In contrast, the dielectric inset operates based on the excitation of the TE_{10} mode, which is horizontally polarized itself. The TE_{10} mode is solely responsible for the antenna's radiation; therefore, there is no need to introduce any asymmetry to induce radiation in the structure, as illustrated in figure 2(c). Moreover, altering the slot aperture is the only way to control the inset's leakage rate. However, in this novel design and combination of slots, the leakage rate can be controlled by adjusting the slot asymmetry (the spacing between the long and nested U-shaped slots) while maintaining the inset space value unchanged.

Acquiring a basic understanding of the difficulties associated with constructing the LWA and the solutions proposed and implemented in this article would be beneficial before embarking on the procedure for developing a wearable, flexible LWA (designed on a layer of denim with permittivity (ε_r) = 1.6 and permeability (μ_r) = 1)). The proposed LWA includes a transmission line-fed rectangular patch. One end of the antenna is used to excite the other end, which is a matched 50-ohm load (figure 1, Stage 1). The fundamental equations that can be used to determine the quadrangular patch's standard and original sizes and the proposed LWA's feed line are given in [29] (since these calculations are fundamental and firm, they are not provided here). Due to the open-stopband (OSB) phenomenon, the LWA can be scanned by utilizing balanced CRLH (Composite Right/Left-Handed) transmission lines, which combine the effects of capacitors and inductors. As a result, the LWA mainly exhibits end-fire or back-fire radiation. It should be mentioned that the open-stopband (OSB) phenomenon is a unique feature of leaky wave antennas that occurs when the signal frequency falls within a specific range, which is called the stopband. In this frequency range, the leaky wave antenna behaves as 'open' or disconnected, leading to little or no radiation. This behavior is in contrast to the regular operation of the antenna, where it radiates electromagnetic waves along its length. The stopband is typically determined by the geometry and characteristics of the antenna structure, such as its dimensions and the material properties. When the signal frequency falls within the stopband, the electromagnetic waves that the antenna would normally radiate are absorbed or reflected within the structure, resulting in minimal radiation [31].

Therefore, improvements should be made to enable outward radiation from the body and in a broadside direction. Several approaches have been proposed to reduce OSB in LWAs, such as uneven elements, impedance matching, and reflection elimination. This problem is fixed by combining longitudinal and nested U-shaped transverse slots on the patch powered by the transmission line (figure 1, stages 2 and 3). In most cases, the electromagnetic waves emitted by these LWAs have polarizations perpendicular to the antenna's and transmission line's longitudinal planes. The goal is to regulate the OSB through reflection canceling. The longitudinal slots strengthen the canceling of OBS, while the transverse slots form a series of left-handed capacitances (CL). Hence, a longitudinal slot is cut from the patch (figure 1, stage 4). The amount of energy released via the slots is determined by the interference of waves that are only partially communicated through the partly reflected surface. These slots modify the fields and currents surrounding the patches. These slots and the fundamentals of a standard LHTL alter the radiation pattern to be more effective on the broadside rather than end-fire or back-fire. At this stage of the design the BW is narrow at working bands of the antenna with two ports. Therefore, it is expanded to four port MIMO antenna (figure 1, stage 5). The four-port leaky wave wearable MIMO antenna can enhance connectivity and mobility with its beam steering capabilities. These features widen BW, ensure higher data rates, improve signal quality, and provide reliable performance in mobile applications. These are crucial for sports, healthcare, military, and everyday applications. Additionally, MIMO systems filter out interference, focusing on the desired signal.

An aperture-coupled slots layer is considered the ground layer to achieve dampened OSB and SAR values (figure 1, stage 6). Furthermore, the feed lines, coupled slots, and the subsequently added layer can function as an aperture-coupled feed for the microstrip antenna, offering advantages such as wider bandwidth, reduced spurious radiations, gain enhancement, and multiple working bands. These features become apparent when observing the reflection coefficient results after cutting the ground by these slots. Moreover, having a growth order between these slots and coupling them with complementary circular SRR can act like a PBG structure, decreasing spurious negative radiation from the patch layer and enhancing radiation efficiency. It is a fact that changing the feeding technique to the aperture-coupled feeding technique can introduce bidirectional radiation. However, it is more for those designs that are conventional microstrip resonators, not the antenna's special structure, which avoids that. As mentioned before, this work's initial aim is to produce a broadside radiation antenna and reduce the side and back lobes. The MIMO antenna is a four-terminal antenna consisting of two-element leaky wave arrays. The arrays were designed to produce a directive major lobe at the broadside, which is both narrow in phi and broad in theta. When an offset phased is introduced into one of the conventional patches, the beam can be tilted off towards the broadside. The radiation pattern of linear arrays can be described and controlled by the relative spacing of the elements in the array. The slots can also alter the amplitude and phase of each element's radiation. However, there is a direct trade-off between the directivity of the major lobe, and the amount of power lost in sidelobe and back lobe radiation after cutting the ground. However, the design intends to keep gain high and sidelobe levels low. The back lobe is tilted off and starts moving towards the broadside after cutting the nested slot on the patches. The periodic cutting of the ground is carried out (following by the principles presented on LWA). The periodic cut of the ground acts like an integrated TM mode surface-wave launcher feed system, which tilts off the possible bidirectional radiation and back lobes. In addition, the patch's nested transverse and longitudinal slots suppressed the OSB issues simultaneously. After integrating the

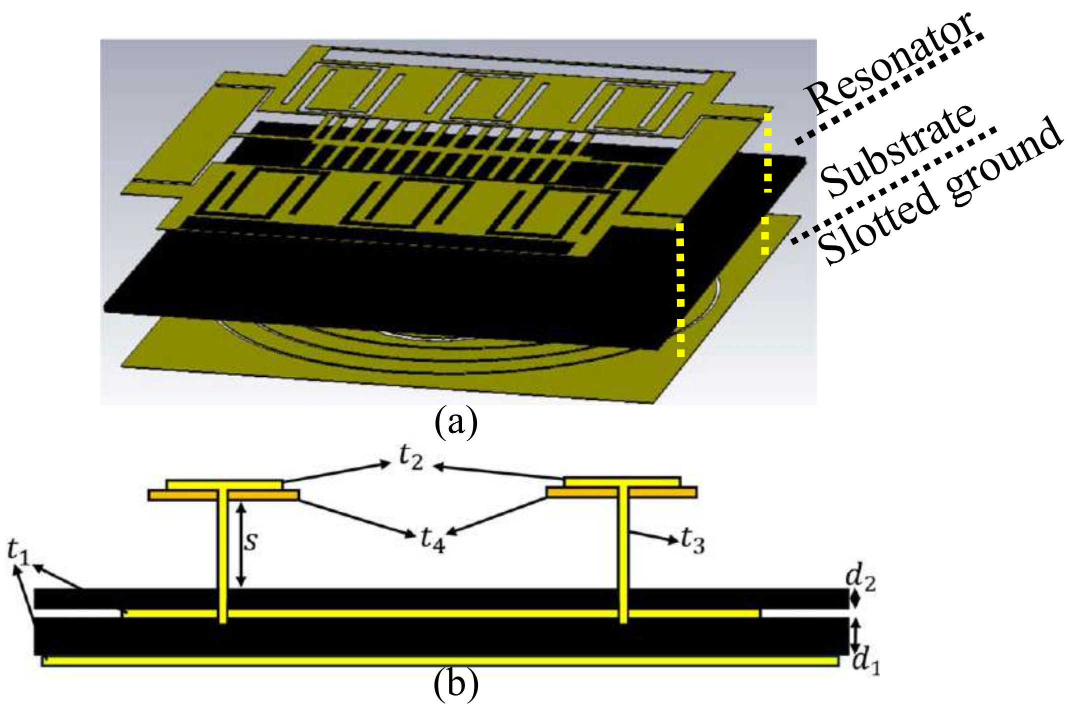

Figure 3. The perspective view of the antenna a: four-port MIMO antenna and b: side view of the antenna.

slots on the patch and the periodic slots on the ground and utilizing ports with optimized spacing, a directive beam can be observed in the far-field, which is scanned through the broadside as a function of frequency. Furthermore, as shown in figure 1(b), the slot-coupled ground layer of the LWA consists of three circular split-ring slots (CSRSs) and three elliptical slots. The CSR and elliptical slots utilize a growth factor based on the desired frequencies. The surface current distribution around the largest slots is more robust at a lower frequency (3.4 GHz). Furthermore, it flows more firmly around the smallest slots at higher frequencies (8 GHz).

Apart from the improvement on the BW and other features mentioned in the previous paragraph, extending from two-port to four-port, MIMO also increases the diversity factors such as diversity gain (DG), array gain (AR), and envelope correlation coefficient (ECC). However, adding another two-port LWA enhances the undesired mutual coupling among the ports when the spacing between these dual-port LWAs is too small. Therefore, the spacing should be increased without significantly enhancing the overall dimensions of the antenna. A coupling reduction technique using neutralization networks offers a better solution for maintaining a low-profile antenna and reducing mutual coupling simultaneously. Hence, neutralization networks consisting of comb-shaped stubs (connecting two large stubs next to the ports and the rectangular patches) are proposed to improve the mutual coupling effects (figure 1, stage 7). It is achieved by suppressing surface wave leakage through the coupled slot ground layer and the patches while having no significant impact on the impedance matching and radiation characteristics. Figure 3 depicts a better perspective of the entire antenna integrated with the spiral buttons. After adding the layer of coupled slot ground layer and cutting the circular split-ring resonators (CSRRs) and elliptical slots from it based on the resonance frequency, another vital factor that should be considered is reducing the mutual coupling between every two ports and enhancing the isolation among them ($S21 < -18$ dB). Various techniques exist to improve the isolation level of MIMO antennas, known as decoupling methods. These techniques include defected ground structures, decoupling networks, electromagnetic band gap structures (EBG), neutralizing lines, parasitic or slot elements, and complementary split-ring resonators (CSRR) [32]. Hence, a combination of these methods is used here. After considering the slot-coupled ground layer as a defected ground structure (DGS) and a photonic band gap (PBG) structure, the decoupling network technique is employed by designing comb networks and stubs (due to the growth order among the slots and the CSRRs). Additionally, two stubs are used to connect the patches to the comb network and each other. The comb-shaped isolating structure is deployed close to the antenna elements, approximately 0.25 mm. The two stubs near the ports (W4, L4) are initially deployed and connected with the long stub. Then, two stubs are connected at the beginning with a length that maintains a space of 0.25 mm between them and the antenna. Subsequently, the remaining parts of the comb are added. Finally, two stubs connect the two patches to the comb network. The isolation level is measured at each step of creating the comb network. To investigate the antenna's characteristics at each of the above designing step, the surface current was checked at each resonance

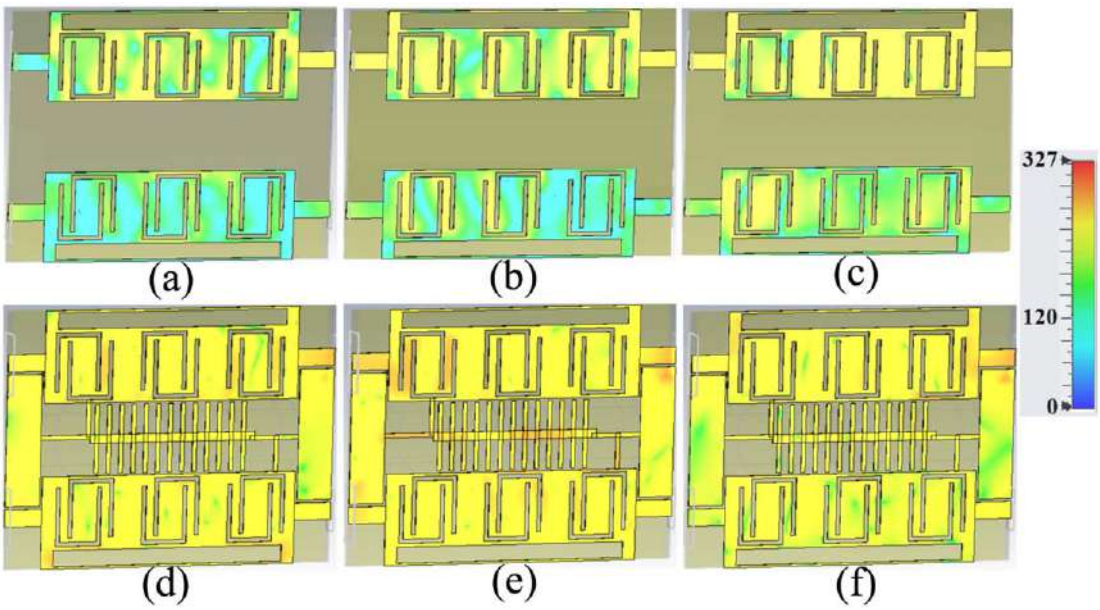

Figure 4. Surface current distribution of the four port MIMO antenna without (a: 3.4 GHz, b: 5.6 GHz, and c:8.5 GHz) and with the comb shape neutralization network (d: 3.4 GHz, e: 5.6 GHz, and f:8.5 GHz).

and pole in the working bandwidth. It demonstrated how the comb network can redistribute the current and shift its focus solely on the patches, thereby affecting the mutual coupling level. For example, at 3.4 GHz, the surface current distribution is observed to flow from the patch connecting ports one and two, extending to another patch through the comb neutralization network. This trend of current distribution is consistent with other working frequency bands.

It is worth mentioning that, following the design of the comb network and the incorporation of the two large stubs adjacent to the transmission lines, two additional stubs are utilized to connect the first patch to the other one, thereby improving the isolation level. However, it is evident that both patches are strongly coupled, as the current flows through the nearby patch and generates an electromotive force (EMF) between them, thereby increasing the mutual coupling of the antennas and promoting the propagation of surface waves through the substrate. The isolating structure effectively suppresses the propagation of surface waves through the ground plane without affecting impedance matching and radiation performance.

Understanding the surface current and electric field distribution around the antenna and resonators is essential. Figure 4 illustrates the current distribution of the surface current of the MIMO LWAs with four terminals. It can also demonstrate how waves propagate from Port 1 through the slots and to the other ports. For instance, strong currents around the nested U-shaped slots should exist at higher frequencies. Conversely, stronger currents flow around the transmission lines at lower frequencies, showing they play an essential role, especially at lower frequencies. This information provides insights into the antenna's behavior and helps understand its performance characteristics. Figure 4 also illustrates the surface current distribution of the LWA antenna after adding the neutralization comb network at different resonances and poles within the working bandwidth. It also demonstrates how the comb network can redistribute the current and shift its focus solely on the patches, thereby affecting the mutual coupling level. However, this coupling level reaches a positive value that is not acceptable. For example, at 3.4 GHz (figure 4(d)), the surface current distribution is observed to flow from the patch connecting ports one and two, extending to another patch through the comb neutralization network. This trend of current distribution is consistent with other frequencies, such as 5.6 GHz and 8.5 GHz. Red and orange are the heist levels of the surface current distribution, and blue and cyan are the lowest current levels.

After explaining the surface current distribution of the LWTA with and without a neutralization network, the parametric study of the essential and practical parameters of the LWTA design should be elaborated thoroughly. The parametric study of the proposed LWTA is indicated in figure 5. The length of the long slot (L_1) affects creating more resonances around 5.6 GHz, 7.25 GHz and a wide BW at higher frequencies around 8.5 GHz. Besides, increasing its length shifts the band to the lower band, and reducing it shifts it to higher bands. The same tendency is followed by L_f and L_p as their increment reduces the frequency and shifts them. Another essential parameter that affects the impedance bandwidth of the antenna is the transversal length of the U-shape slot (L_2). This parameter also follows the trend of the other lengths, widening the BW around 8.5 GHz and

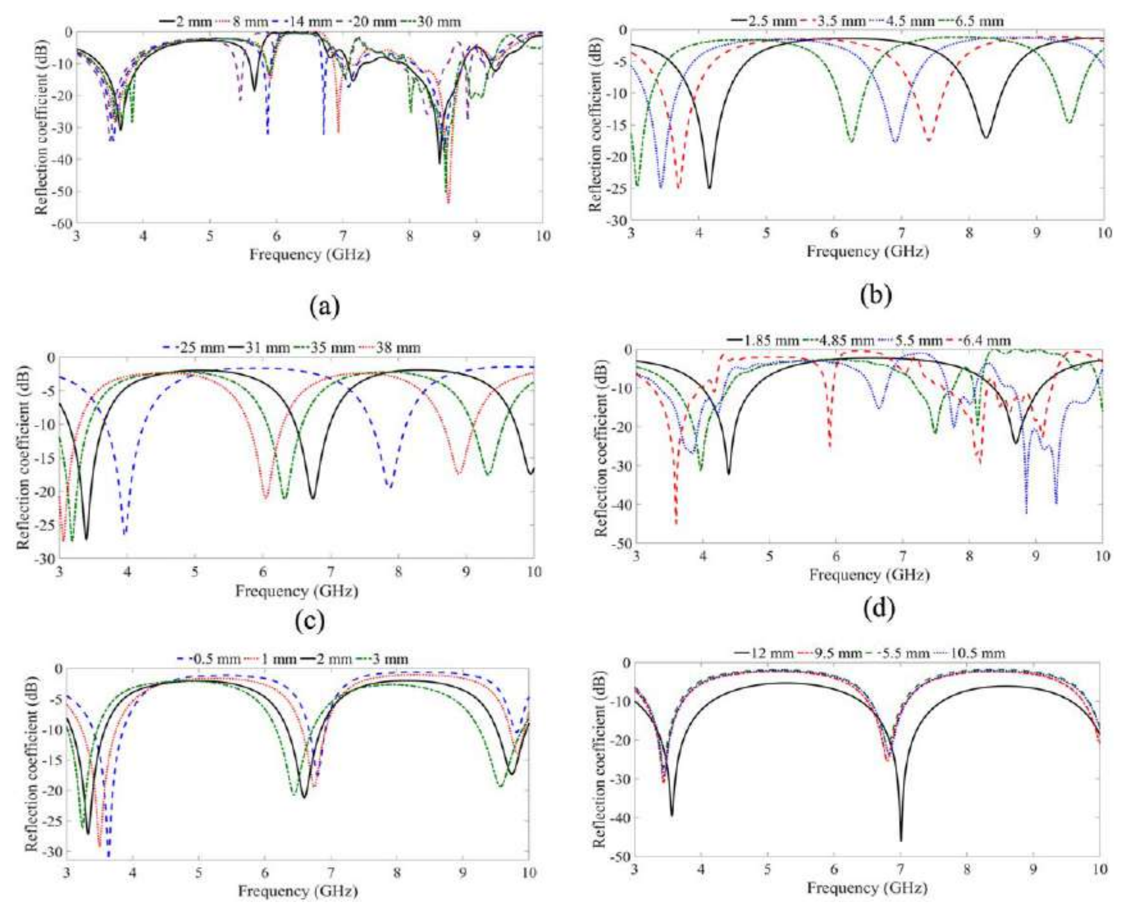

Figure 5. Parametric study of the LWA antenna : a) L_1, b) L_f, c) L_p, d) L_2, e) W_f, and f) W_p.

Table 1. The design parameters of the proposed antenna (mm).

Parameters	Values (mm)	Parameters	Values (mm)	Parameters	Values (mm)	Parameters	Values (mm)
L_s	40	W_s	30.00	g_1	0.50	r_1	0.50
L_p	31	W_p	10.75	g_2	0.50	r_2	6.50
L_f	4.50	W_f	2.00	g_3	0.50	r_3	4.25
L_1	28.00	W_g	38.50	g_4	0.60	r_4	6.25
L_2	6.40	W_1	1.90	g_5	0.25	r_5	8.25
L_3	6.00	W_2	5.00	g_6	0.50	b_2	16.00
L_4	15.30	W_3	1.25	a_1	9.25	b_3	18.00
L_5	5.40	W_4	4.20	a_2	11.25	t_2	0.18
L_6	3.75	W_5	0.50	a_3	13.25	t_3	0.50
L_7	3.5	b_1	13.50	t_1	0.07	t_4	0.50
d_1	0.50	s	8.75	L_8	8.00	L_9	6.60
L_{10}	5.25	L_{11}	4.25	L_{12}	3.25	L_{13}	3.75
L_{14}	4.75	L_{15}	5.70	W_6	0.60	W_7	0.40
W_8	0.25						

higher bands. However, when it is too short, less than 2 mm, the middle bands are suppressed entirely, and the total band is shifted to the higher band. W_f unlike W_p affects widening the BW at the operating frequency and shifts to higher band by reducing its values. After parametric study and optimization of each design parameter, they are presented in table 1.

Figure 6 indicates the reflection coefficient results of the MIMO LWA for each port after adding the other ports. It also shows that the MIMO LWA achieves resonance around 3.4 GHz when only ports 1 and 2 are active. Upon activating the other ports and applying the loading on the LWA, it is essential to note that the LWA used here does not include the neutralization network and the coupled slots ground layer. Instead, it features a complete layer of ground. Consequently, additional resonances are observed at higher bands after activating the

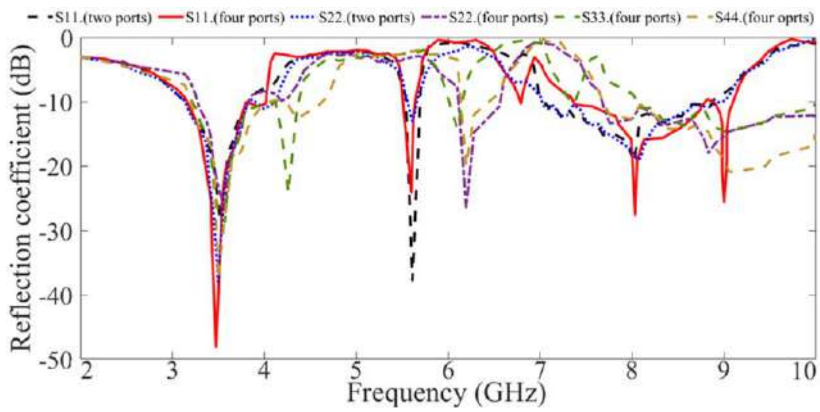

Figure 6. Reflection coefficient result for each part stage of the proposed MIMO antenna considering one to four ports.

other ports. However, the antenna's radiation efficiency, gain, and other desired MIMO characteristics have not yet met the requirements. Therefore, modifications to the loadings and other design aspects are necessary to improve the antenna's characteristics.

2.2. Detachable Button Antennas with a Front Spiral Resonator and CHSRR

Planar spiral antennas have found extensive use in innovations involving bidirectional radiation, wideband coverage, and circular polarization, primarily due to their design's frequency independence [33]. However, it becomes necessary to have an antenna that exhibits unidirectional radiation properties when it comes to wearable antennas and applications in Wireless Body Area Networks (WBANs). The challenge with planar spiral antennas is that they produce radiation in two directions. Several viable options exist to convert the bidirectional radiation of a planar spiral antenna into unidirectional radiation, including backing the antenna with an absorbing cavity, utilizing reflecting synthetic electromagnetic material as a reflector or using a perfect electric conductor (PEC) cavity [34, 35].

The spiral button antenna is constructed using a round PTFE (Polytetrafluoroethylene) substrate with specific dimensions and properties. The substrate has a permittivity of 2.1, a loss tangent of 0.001, and a thickness of 0.508 mm. Firstly, we considered the formulas stated in [36] to design an Archimedean spiral radiator that operates in free space at the frequency of 3.4 GHz. Parameters such as r_1, r_2, g_2, and w_3 can be obtained using those equations. The effects of these design choices on the antenna's characteristics were determined by performing parametric sweeps in the 3D CST Microwave Studio environment. Both the expansion rate and the inner radius r_{in} were included as variables in these sweeps. The comprehensive spiral design process and the relevant parameters are also carried out. Therefore, we will provide a brief overview of the calculated parameters for this design and discuss the effects of adding the CHSRs. For instance, when the r_{in} parameter is set to 1.2 mm, the length of the feeding area is still significantly shorter than the length of the active region's 10 GHz ring. However, the deterioration becomes more noticeable as the r_{in} parameter increases beyond 1.2 mm. Therefore, it is advisable to select the smallest available r_{in} parameter. Before changing the ground to the CHSRRs, a parametric study is presented to show the important design parameters of the spiral antenna, as presented in figure 7(a). Figure 8(a) depicts the parametric study of the gap between each turn of the spiral antenna. It shows that when it is less than 1, no dramatic changes occur except the slight shift of the resonance to the lower band by the increase. The number of spirals follows the same trend for turns (n) as enhancement in n increases the resonance and shifts the bands to the higher band as shown in figure 8(b). Last but not least, the internal radius of the spiral (r_1). An increase in the internal radius of the spiral enhances the BW and slightly shifts it to the lower band as illustrated in figure 8(c). However, it will enhance the total diameter of the spiral.

The ground plane has an impact on the far-field pattern of an equiangular spiral antenna, causing a limited bandwidth that operates in only one direction. Therefore, the bottom layer of the substrate was loaded with CHSSRs to enhance the bandwidth of the spiral button antenna. The thickness of the substrate and its respective constants affect the BW, efficiency, and gain. In addition, the fringing field at the edge of the circular substrate and the surface waves around the spiral degrade the BW and efficiency and gain when the ground is in the complete layer. Therefore, the bottom layer of the substrate was loaded with CHSSRs to enhance the bandwidth of the spiral button antenna. The CHSRR, like any other SRR, is a metamaterial structure that creates negative index characteristics (μ, ε, n) and passbands and stopbands at the selected frequencies. These passbands

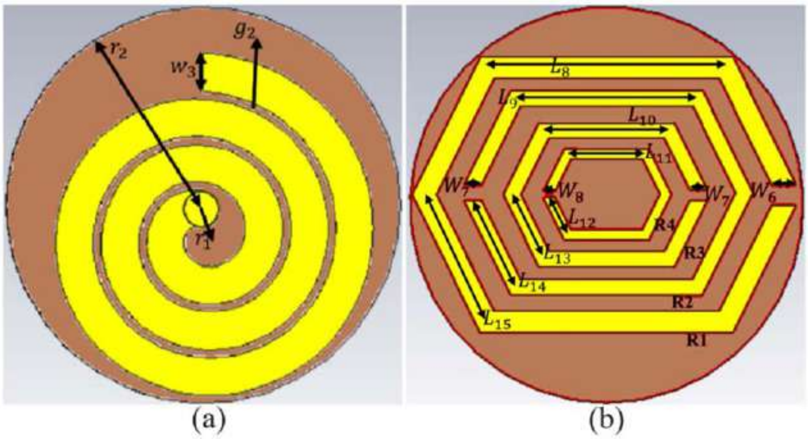

Figure 7. The button antenna's simulated model (a: front view, b: the rear view).

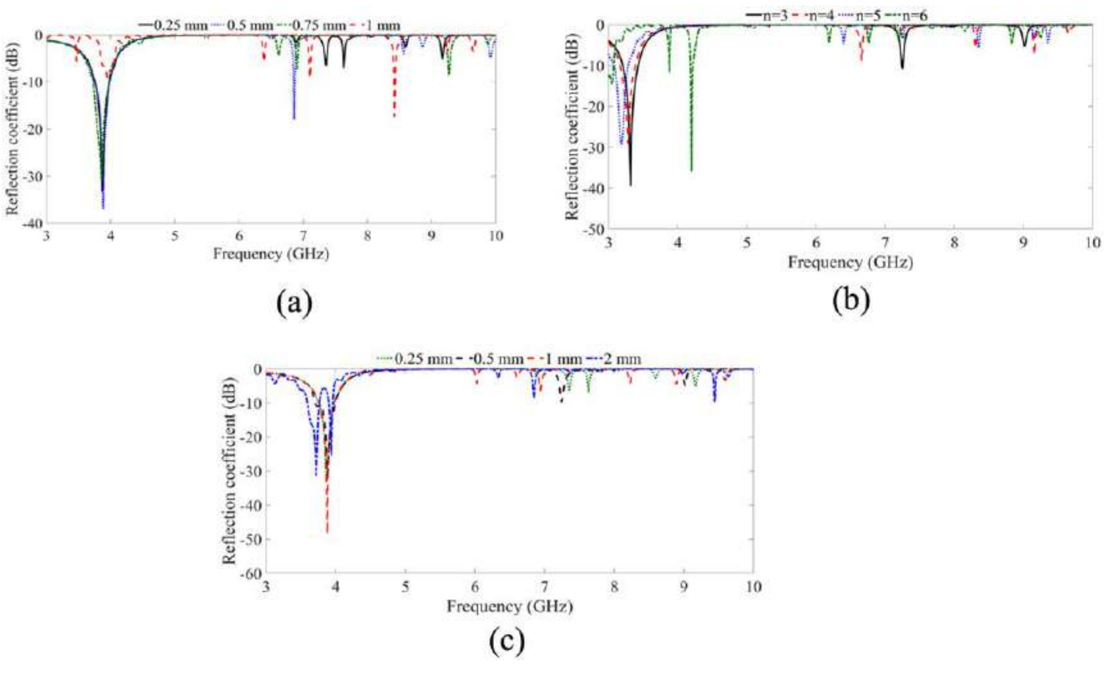

Figure 8. The button antenna's parametric study: a) g_2, b) the turns (n), and c) r_1.

enhance the working BW and gain at the desired resonances. Optimizing their structure also helps; for instance, a small gap in SRR can show better performance. Later, these metamaterials' negative index characteristics are extracted from the S-parameters of the CHSRR structure using the Nicolson-Ross-Weir (NRW) technique.

The spiral is initially driven to acquire the lowest resonance, approximately 3.4 GHz, and to achieve circular and dual polarization properties for the antenna. The rear ground of the spiral button antenna is illustrated in figure 7(b), while figure 7(a) showcases the antenna itself. The working principles of the CHSRR can be understood with the help of comparable circuit designs that illustrate the concept of SRRs. Therefore, a brief explanation of the equivalent circuit design is given below. The proposed CHSRR is a nested structure comprised of a combination of SRR and complementary SRR, considering their equivalent circuit. Since the CHSRR has a shape like a circle with six edges, the equivalent circuit for complementary circular SRR (CSRR), an inductor parallel to two series capacitors, is utilized, as shown in figure 9. It is also a nested structure having two complementary HSRRs. At the design's initial stage, the space between the center of the circular substrate and the hexagonal rings are the same for each side of the HSRR as well as their thickness (w). Therefore, the internal and external radius of the hexagonal shape is the same for each of the two CHSRRs.

The Ls_1 and Ls_2 in figure 9 denote the self-inductance of the SRR structure, C_0 defines the total capacitance between the rings, $C_0 = 2\pi r_0 C_{pul}$ where r_0 (R_2, R_4) is the effective radius of the rings, and C_{pul} is the per-unit-

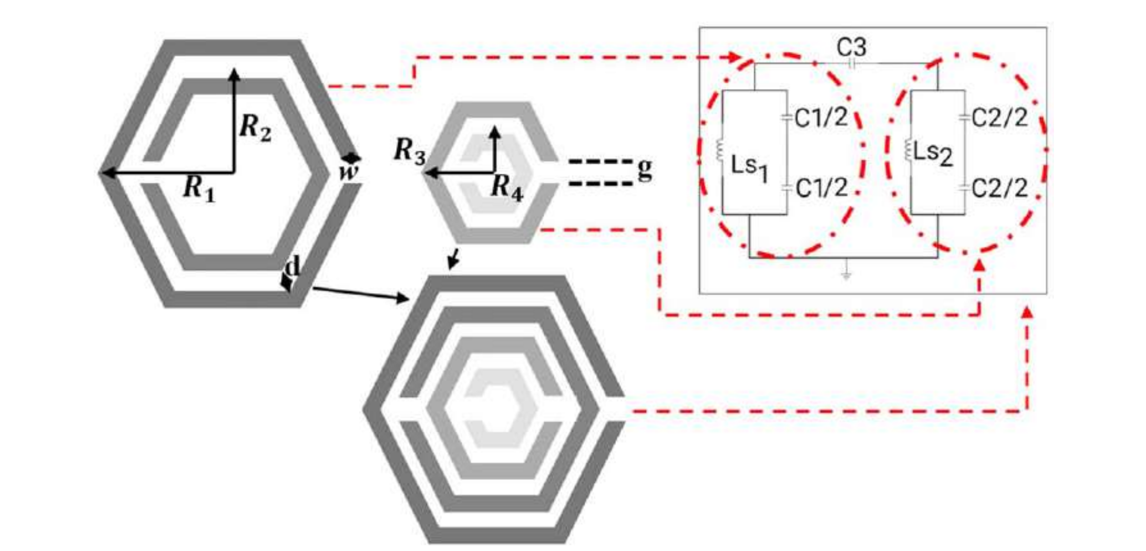

Figure 9. The equivalent circuit of the CHSRR metamaterial unit cell.

length capacitance. C_s, the resultant capacitance is given by $C_s = C_0/4$. The resonance frequency of a CHSRR is predicted from the formula $f_r = 1/2\pi\sqrt{L_s C_s}$, the Ls and Cs are obtained by the formula. C1/2 is obtained by two parallel capacitors as C || C_{g1} and C || C_{g2}. Applying general trigonometry to figure 8 assuming the same gap for all CHSRR called *g*, we also assume r as the effective radius as presented in [37], by equating to any side of the hexagon it will give us *g/*6. Therefore, we will have:

$$r_0 = r - g/6$$

The self -inductance similarly as presented for circular SRR, L_s can be analytically expressed slightly different as:

$$\text{Ls} = 0.00508.l(\log\frac{4l}{w} - 2.636)$$

Similar to the circular SRR, the resultant capacitance for the CHSRR can be extracted slightly different as follows:

$$\text{Cs} = \left((3+\beta)^2 - \left(\frac{\Delta}{r}\right)\Big/2(3+\beta)\right) \times rC_{pul}$$

Where, $l = 6 \times r_0$ is the effective length of the ring, *w* is the width of the ring, ε_0 is the absolute permittivity, $\beta = C_g/rC_{pul}$, C_g is the capacitance due to the gaps (*g*), and *g* is the gap between the split. Since the substrate has a thickness of *h*, the parallel plate can be considered so that $C_g = \varepsilon_0\varepsilon_r wh/g$ and the $C_{pul,}$ which has the effect of length and the distance between the rings, can also be extracted as: $C_{pul} = \varepsilon_0(\varepsilon_r + 1/2)(\varepsilon(\sqrt{1-\sigma^2})/\varepsilon(\sigma))$. Using the previous equations and the rest of the equation presented by [37], the resonant frequency of the CHSRR can be obtained. It should be noted that these equations are for each section of the equivalent circuit shown in figure 8. For example, Ls1 is for the two bigger rings, and L_{s2} is for the smaller two rings circled by a dashed red circle. A series capacitor should be considered since these CHSRRs are nested. These coplanar and parasitic components exhibit their impact on total magnitude. The above-discussed effect has been studied by simulating the circuit in Advanced Design Systems (ADS) software. The initial values of most circuit components are obtained by using the presented above and the rest of the equation presented in [37]. The equivalent circuit is drawn using ADS, considering these initial circuit component values. Then, the final component values were determined by tuning the component values in ADS so that the S_{21} of this circuit could be well-matched with the CST output. The magnitude of S_{21} can be adjusted by adequately tuning the series resistances associated with each inductor. However, in drawing simplicity, these values are ignored in the equivalent circuit. This is due to the fact that the proposed design is a modified form of a standard split ring resonator in which various inductive and capacitive values are distributive in nature, and inter-ring distance is not constant at every place. Thus, the actual values obtained from the formulas should be optimized. The optimized values of these parameters are presented in table 1.

To simulate the metamaterial structure along with the spiral, an electromagnetic force (EMF) is measured at the CHSRRs when an external magnetic field is applied along the *Z*-axis. The current source of this EMF is the connection between two annular metal rings. The current flows from one ring to the next through the

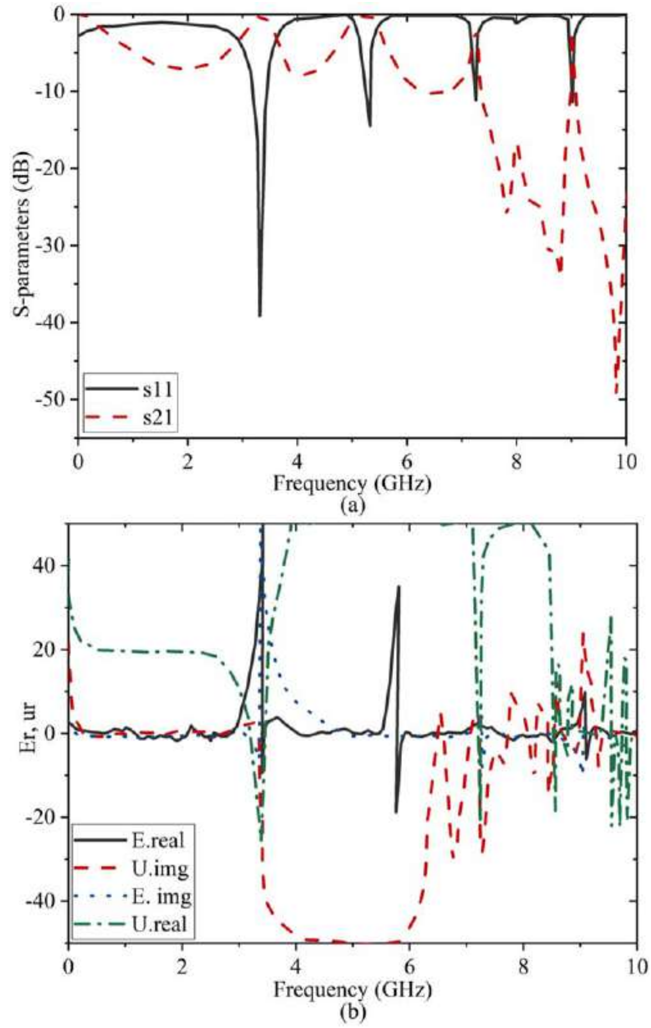

Figure 10. (a) the S-parameters, and (b) the extracted permittivity and permeability results of the CHSRR.

capacitance formed between the interior gaps of the rings. In figure 10, the S-parameter results are presented, along with the retrieved permittivity (ε_r) and permeability (μ_r) values (both real and imaginary sections) of the CHSSR unit cell.

The larger CHSRR and the three smaller ones have different resonance frequencies (f_r), ranging from 5.6 GHz to 7.2 GHz and 8.7 GHz. The CHSRR procedure was modeled in a virtual microwave studio for more assurance (CST MWS). Initially, the CHSRR structure was positioned near the power line. The smaller CHSRRs have resonances in 8.65–9.5 GHz and 5.55–5.65 GHz, while the largest CHSRR has a resonance in the 3.35–3.45 GHz range. Furthermore, the −2 dB transmission coefficients indicate excellent signal-to-noise ratios (see figure 10(a)). At these desirable frequencies, the refractive index approaches zero. Each unit was developed with a specific frequency in mind, and the four CHSRRs were introduced in a particular order based on their frequencies. They function similarly to a photonic band gap, suppressing unintended resonances while amplifying the desired ones. Additionally, when the space within the spiral is constrained, it prevents surface waves and undesirable fringing fields from reaching the button antenna [38].

Figure 11 illustrates the surface current distribution of the CHSRRs in the presence of the spiral. The surface current distribution assessment of the spiral button at each selected resonance frequency gives us a visualization of the current flow through the spiral and CHSRR and how their capacitive separation can affect it. It also demonstrates the parasitic current sharing between the two CHSRRs, with the larger one acting as the primary conductor. Furthermore, it indicates the suppression of surface current after adding CHSRR cells behind the spiral, resulting in improved radiation characteristics of the spiral button. The design of the four CHSRR cells involves utilizing periodic growth factors. Each ring functions as a capacitor in series with a resistor and an inductor. A coupling capacitor is used to establish communication between the rings. It is worth mentioning that the length of each CHSRR is calculated based on its corresponding resonance frequency. The impedance matching of this structure can be checked and optimized by observing the changes in the Smith chart whenever

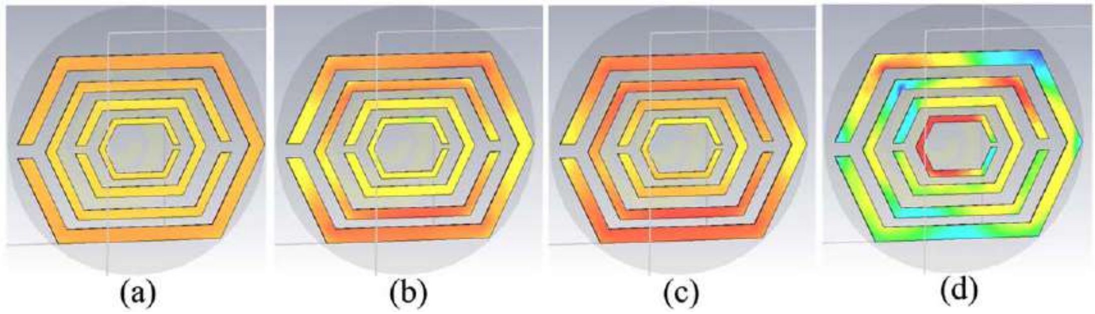

Figure 11. The surface current distribution (SCD) of the CHSRRs (a: 3.4 GHz, b: 5.6 GHz, c: 7.2 GHz, d: 8.2 GHz). (a) depicts that the current is stronger around the biggest ring at 3.4 GHz. Then, it becomes strong around the second two rings at 5.6 GHz in figure 10(b). the current follows the same tendency after adding the other two rings at 7.2 GHz and 8.2 GHz.

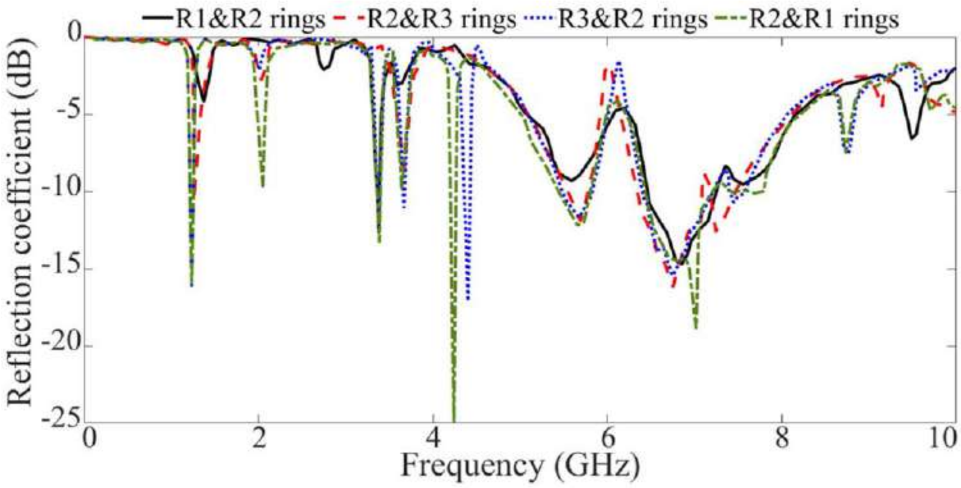

Figure 12. The reflection coefficient results of the CHSRRs for each ring.

another ring is added. Permittivity and permeability are negative indices of the metamaterial (MTM) structure, indicating how much it influences the button antenna and LWA at specific frequencies. Critical variables have been optimized to meet the required specifications after studying the spiral button antenna's bandwidth, gain, radiation pattern, and polarization state.

Figure 12 displays the reflection coefficient results of the button antenna when combined with the spiral and each ring. The resonances associated with each split ring are observed to be active when all four CHSRRs are present. Additionally, the incorporation of MIMO LWA assists in eliminating an undesired resonance. Combining the antenna with the LWA enhances the directional gain, beam scanning capability, and broadside radiation in the outward direction.

3. Result and Discussion

To facilitate understanding, the antenna's performance for on-body and off-body scenarios is presented in separate results subsections. Firstly, the evaluation is conducted with the antenna in the air (off-body) to assess the antenna's performance in free space. Next, the antenna is assessed close to a person to evaluate its effectiveness when worn. Figure 13 displays the preliminary reflection coefficient data at various stages of the antenna design process, both before and after integration (figure 1). The reflection coefficients are presented for the MIMO LWA and button antenna in various configurations, including with and without the coupled slot layer, the matching stubs (also called neutralization network), after incorporating the button antenna, and after implementing layered U-shaped slots. Adding four hexagonal rings behind the spiral button antenna allows for four resonances (shown in figure 13). When a complementary hexagonal split-ring (CHSR) is added to the button antenna, the inductive loading causes the resonances to shift towards lower frequency ranges.

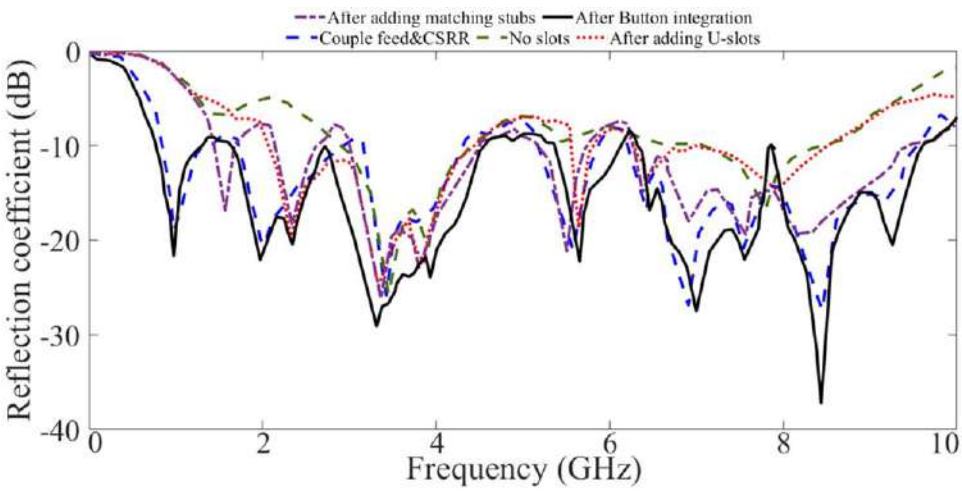

Figure 13. The reflection coefficient results of the antenna at a different stage of the design.

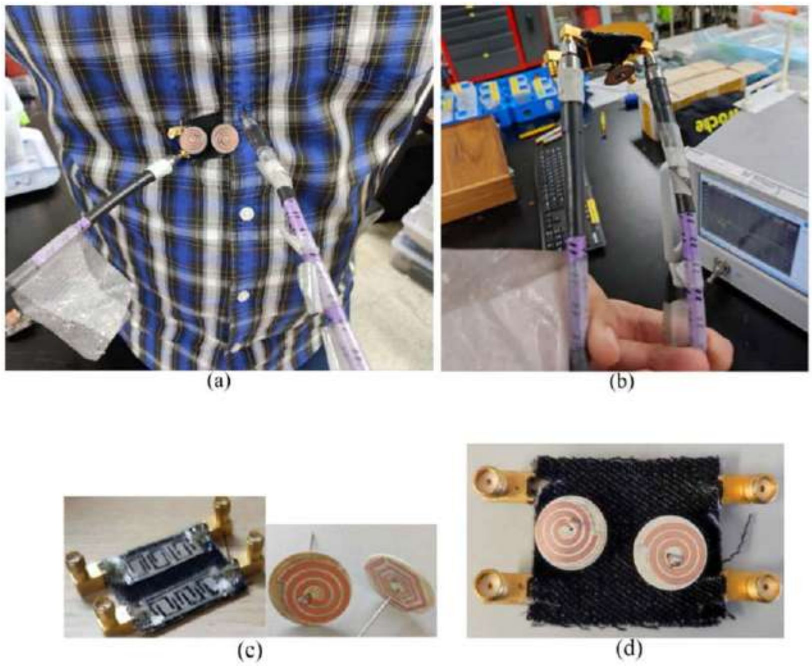

Figure 14. The measurement setup of the proposed antenna in both air and on-body (a: antenna on chest; b: measurement in free space; c: fabricated antenna before integration with buttons and last layer; d: fabrication of final design).

Consequently, the button antenna is combined with the MIMO system. The pins of the button antenna are connected to specific points on the MIMO system to prevent the operating bands from deviating from the specified bands. It should be mentioned that they are not connected to the naturalization network.

As a result, the MIMO and button antenna integration demonstrates improved performance compared to the previous phases. This integration showcases stable radiation performance, and the article further discusses beam width. The functioning bands are successfully achieved even after the integration. Moreover, when combining the button antenna with the MIMO antenna, all the required frequencies of 0.86–2.75 GHz, 2.9–4.85 GHz, 5.75–6.15 GHz, and 8–9.85 GHz are attained.

3.1. Off-Body Investigation Results

Models presented in figures 1 and 14 were developed to validate the theoretical concepts. The antenna model was created using denim and ShieldIt conductive textiles. The two layers are adhered together using a plastics-to-textiles glue. The S-parameters of the antenna were measured using a two-terminal HP 8510C vector network

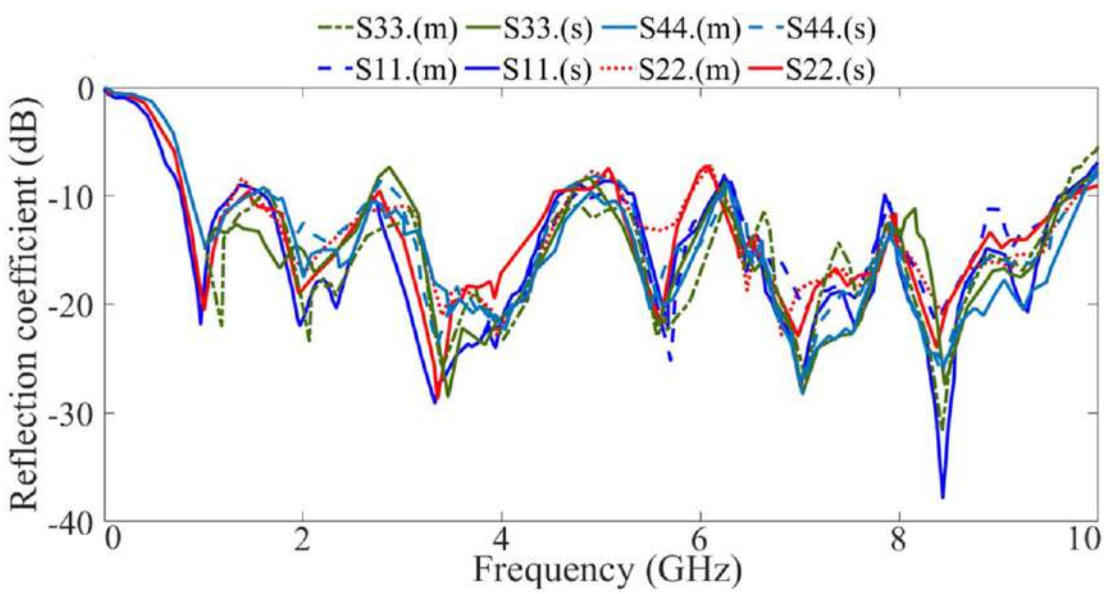

Figure 15. The antenna's reflection coefficient findings in the air (off-body) ('s' is a simulation, 'm' is measurement).

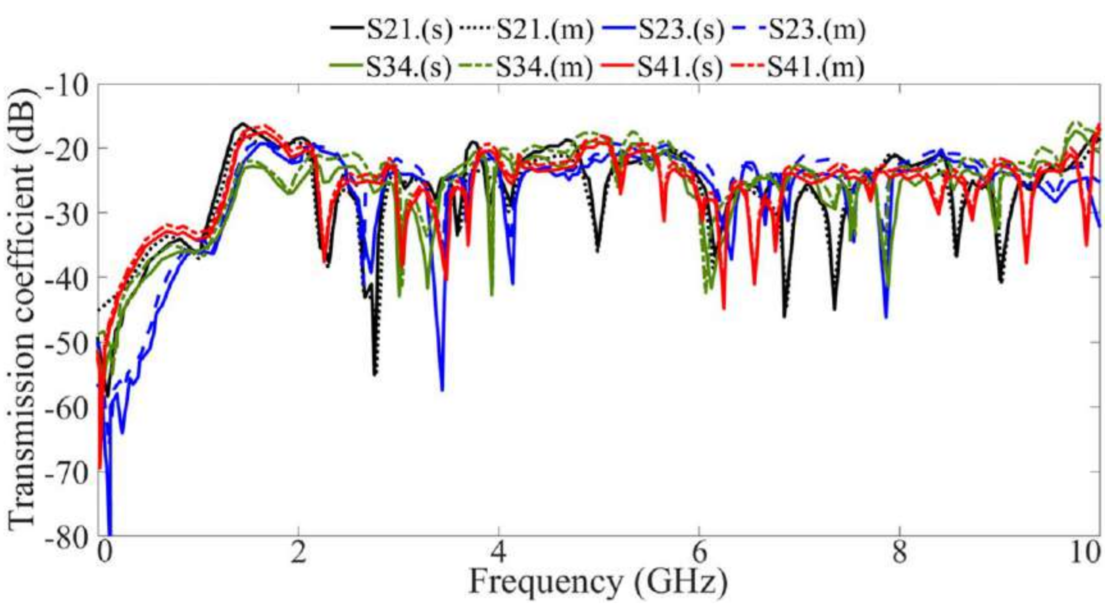

Figure 16. The antenna's transmission coefficient results in the air (off-body) ('s' is a simulation, 'm' is measurement).

analyzer (VNA) after calibrating the antenna. The measurement process was conducted in four stages, connecting Ports 1 and 2 and progressing to Ports 3 and 4.

Two antennas were employed, with one connected to the first terminal of the VNA and the other connected to its second terminal, to capture the measurements. After calibrating the antenna and determining the frequency band, the antenna's S-parameters, including reflection and transmission efficiencies, were measured (refer to figures 15 and 16, respectively). Figure 15 illustrates a comparison between the simulated and measured reflection coefficients. The predicted results closely match the actual measurements. However, some irregularity is observed in the upper band due to its relocation. Nevertheless, the antenna still functions as intended when utilized within the correct band and context. The resonances of each port are exhibited almost within the required frequency bands of 0.86–2.75 GHz, 2.9–4.85 GHz, 5.75–6.15 GHz, and 8–9.85 GHz, which are essential for the prementioned applications. The transmission coefficient results of the MIMO antenna prove the acceptable range of less than −22 dB at most of the BW, showing an acceptable isolation level. Besides, not too many disagreements exist between the ports.

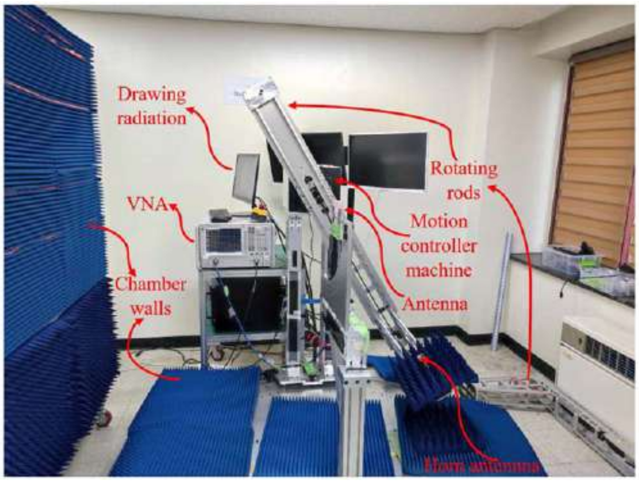

Figure 17. The radiation pattern measurement setup.

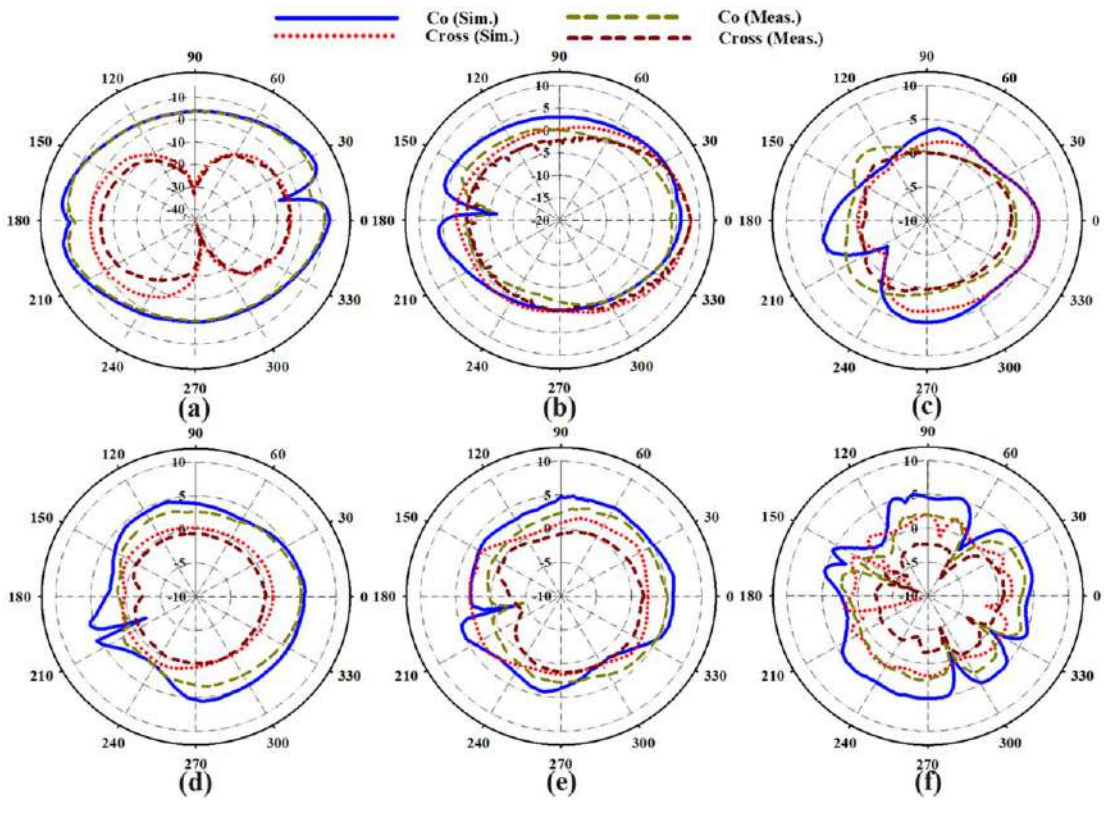

Figure 18. The radiation pattern of the antenna (simulated (sim) and measured (meas) cross and co-polarization) at a: 2.4 GHz, b: 3.4 GHz, c: 3.8 GHz, d: 5.6 GHz, e: 7 GHz, and f: 9 GHz.

The antenna's radiation pattern was also examined by utilizing a vector network analyzer (VNA), a personal computer (PC), and an anechoic chamber within the operating bandwidth of 0.1–10 GHz. Subsequently, the radiated field strength of the antenna was evaluated. We connected a reference horn antenna to a rotating rod linked to a power meter to measure the radiation pattern. The wheels on the left vertical wall of the chamber, as depicted in figure 17, were used to shift the wall to the right. Simultaneously, the spinning rod was readjusted to facilitate measurements on the right side of the chamber. Instead, the proposed antenna was securely attached to a significant pole section. A motion controller was employed to rotate the rod in increments of 3 degrees simultaneously. After each rotation, a pause was introduced to record the data, followed by resuming the cycle. The power output from the computer was recorded, and MATLAB was used to generate the radiation pattern. Additionally, the antenna was rotated in the elevation plane, and the measurement process was continued.

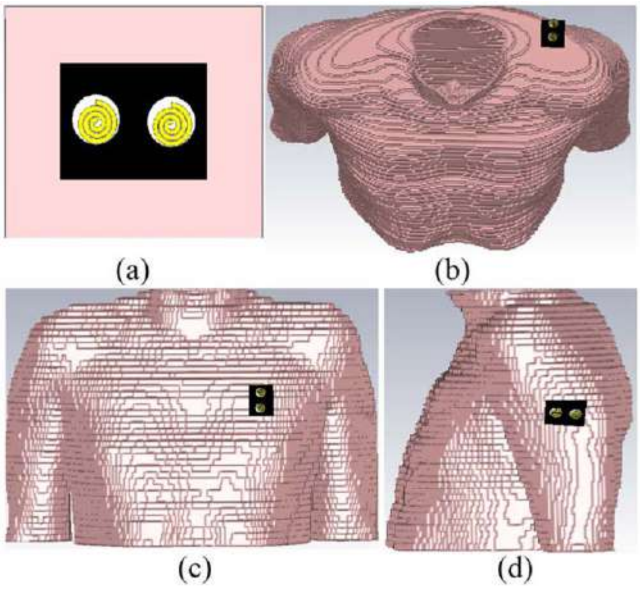

Figure 19. The on-body simulation setup: (a) Human tissue, (b) the shoulder, (c) the chest, and (d) the arm.

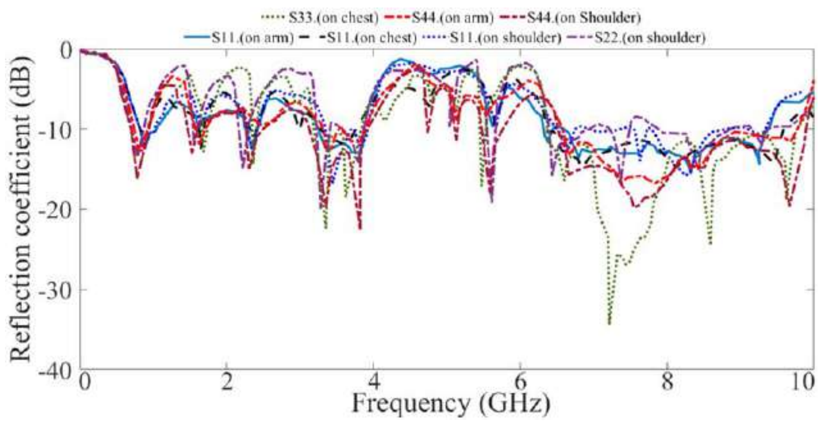

Figure 20. The reflection coefficient results of the proposed antenna on voxel.

Figure 18 displays the measured and simulated cross-polarized and co-polarized radiation patterns for the antenna. The simulated and experimental results showed a slight, insignificant difference, which can be attributed to tolerances in fabrication during the manufacturing process. The recommended antenna's radiation pattern is outward to the body, with the main lobe pointing nearly at 0°. This characteristic makes it a promising choice for wearable antenna systems and communication. Besides, the cross-polarized radiation pattern level is less than the co-polarized, which is desired for any dual-polarized or CP antenna. In addition, the two port arrangements (two ports arrangement become a four-port MIMO) of the proposed antenna also improved the cross-polarization level to minus levels.

3.2. On-Body Investigation Results

Throughout this subsection, we discuss the on-body performance of the suggested antenna in terms of S-parameters, radiation pattern, gain, efficiency, axial ratio (AR), and SAR value. Figure 19 depicts the simulated configuration for on-body conditions, specifically the voxel arm, chest, and shoulder, to examine the antenna's features more naturally. Figures 20 and 21 display the simulated S-parameter results of the antenna for voxel body scenarios. All the necessary frequencies and bandwidths are present and operational. However, physiological characteristics and layers cause a more significant shift in the bands within the voxel compared to the tissue. Additionally, the voxel results exhibit more band notches than the results in free space. Despite that, the required frequency bands function as expected within the simulation. The transmission coefficient between any two ports remains below −20 dB across the usable bandwidth, ensuring excellent port isolation.

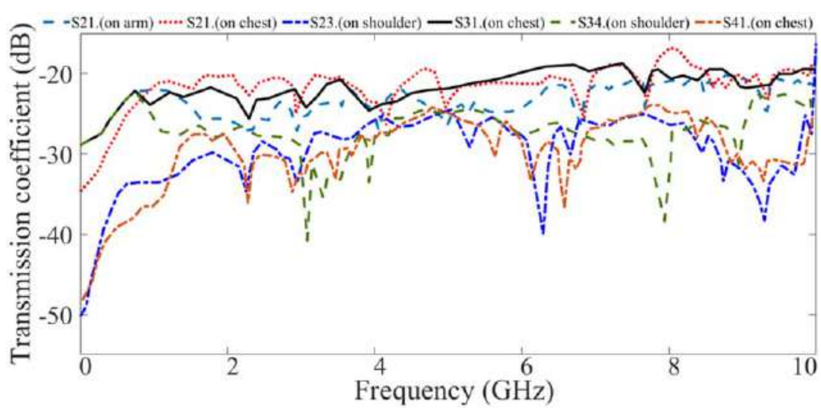

Figure 21. The transmission coefficient results of the proposed antenna on voxel.

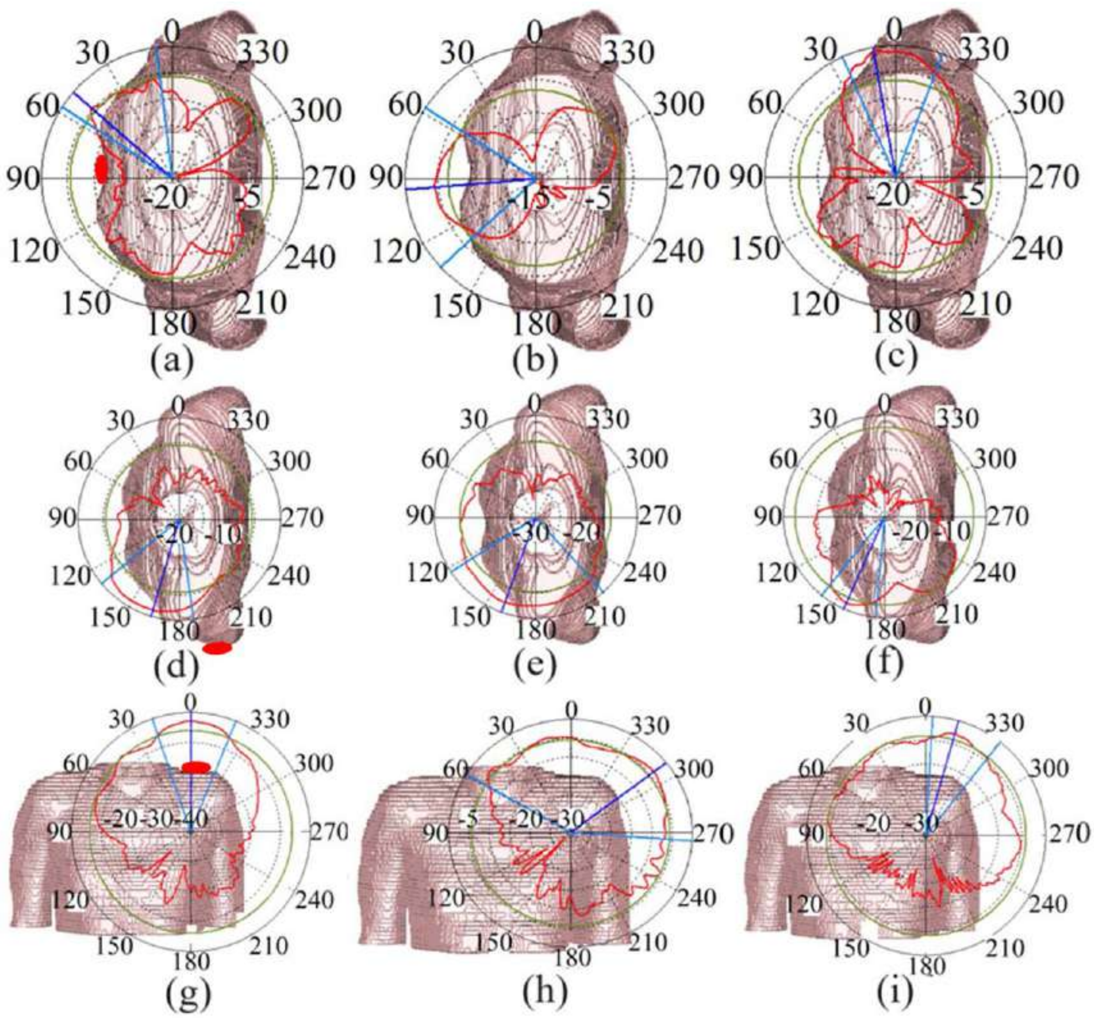

Figure 22. The simulated radiation pattern of the antenna on the chest (at a: 3.4 GHz, b: 5.6 GHz, c: 8.2 GHz), on the arm (at d: 3.4 GHz, e: 5.6 GHz, f: 8.2 GHz); and on the shoulder (at g: 3.4 GHz, h: 5.6 GHz, i: 8.2 GHz). (the red elliptical shape is the location of the antenna on the body).

The antenna's radiation pattern on the human body is illustrated in figure 22, corresponding to different locations such as the chest, arm, and shoulder. It is worth noting that, to streamline the evaluation process and reduce the number of mesh cells in the CST Studio, only half of the body voxel (from the neck to the hip) is included in the simulations. When the antenna is mounted on the voxel body, it emits radiation in all directions except inward. At lower frequencies, the radiation is predominantly focused outward in the user's chest, while at

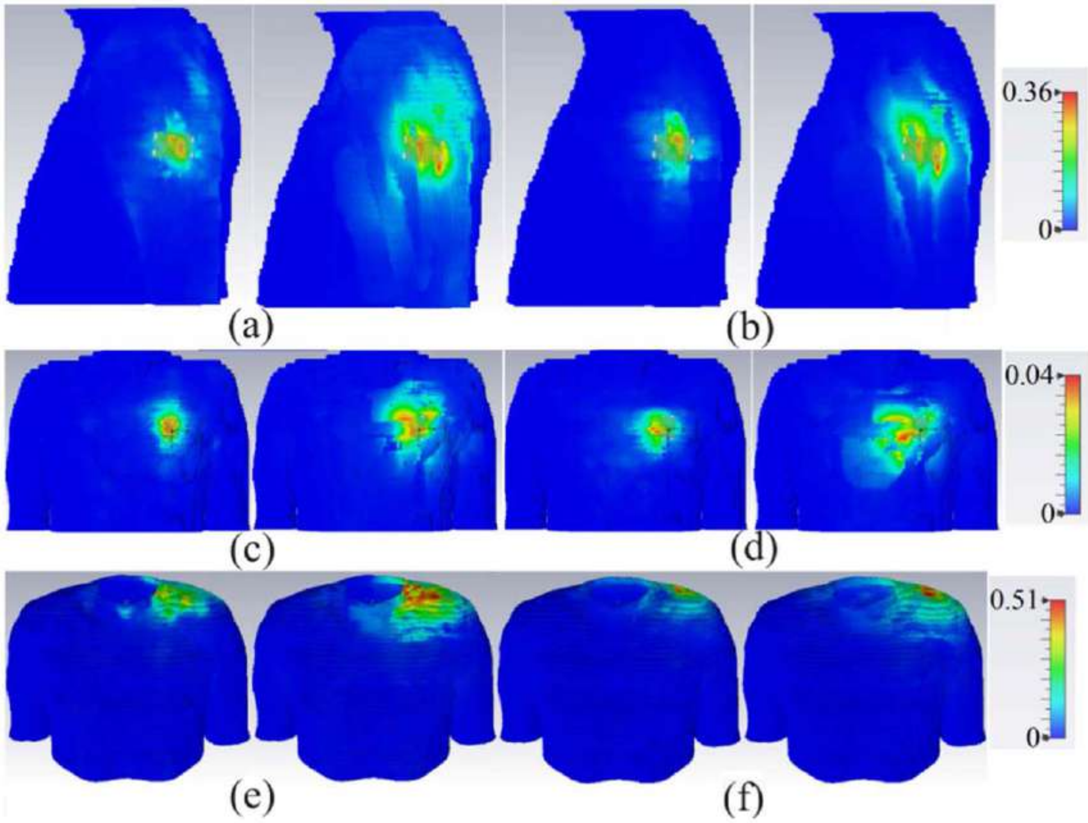

Figure 23. The proposed antenna's SAR evaluation on the arm (a: 3.4 GHz, 1g/10g; b: 5.6 GHz), on the chest (c: 3.4 GHz, 1g/10g; d: 5.6 GHz), and the shoulder (e: 3.4 GHz, 1g/10g; f: 5.6 GHz).

Table 2. The comparison of the antenna's performance in air, arm, chest, and shoulder.

	f_r (GHz)	3.4	5.6	7.2	8.2
Free space	Gain (dBi) Sim/Meas	4.7/4.1	5.81/5.24	8.5/8.10	7.24/7.63
	Eff (%)	85	90	92	89
On chest	Gain (dBi) Sim/Meas	4.26/3.95	6.11/5.15	7.34/7.45	6.9/6.23
	Eff (%)	85.81	88.99	90.12	90.14
	SAR (1 g/10 g)	0.03/0.045	0.035/0.025	0.04/0.045	0.004/0.025
On arm	Gain (dBi) Sim/Meas	4.35/-	6.82/6.51	7.44/-	6.95/-
	Eff (%)	87	89	91.23	90.11
	SAR (1 g/10 g)	0.031/0.021	0.36/0.191	0.031/0.021	0.36/0.191
On shoulder	Gain (dBi) Sim/Meas	5.05/-	7.18/-	7.45/-	7.10/-
	Eff (%)	86	91.5	91.33	90.45
	SAR (1 g/10 g)	0.512/0.534	0.36/0.355	0.335/0.435	0.236/0.155

higher frequencies, it shifts within the range of 30 to 60 degrees (as depicted in figure 22). Similarly, the arm and shoulder radiation exhibits an outward pattern. For the arm, the radiation is primarily concentrated in the 160–180 degree range, while for the shoulder, it is around 120 degrees. Furthermore, the radiation patterns remain consistent for higher and lower frequency bands directed away from the body.

The SAR factor should be considered when assessing the performance of a wearable antenna and associated telecommunications. According to American and European guidelines, the SAR values must be lower than 2 and 1 W/kg^3. Figure 23 displays the impact of the suggested antenna's SAR variation on voxelated human tissue (arm, chest, shoulder). Even at an antenna separation of 5–8 mm, the readings did not deviate significantly from the norm. Table 2 lists the precise values of the SAR factor. The SAR values are well within the safe zone. Therefore, we can conclude that the human voxel body and tissue do not significantly affect the antenna. The antenna and human tissue have a separation of 5 mm, while the separation between the antenna and voxel is 8 mm.

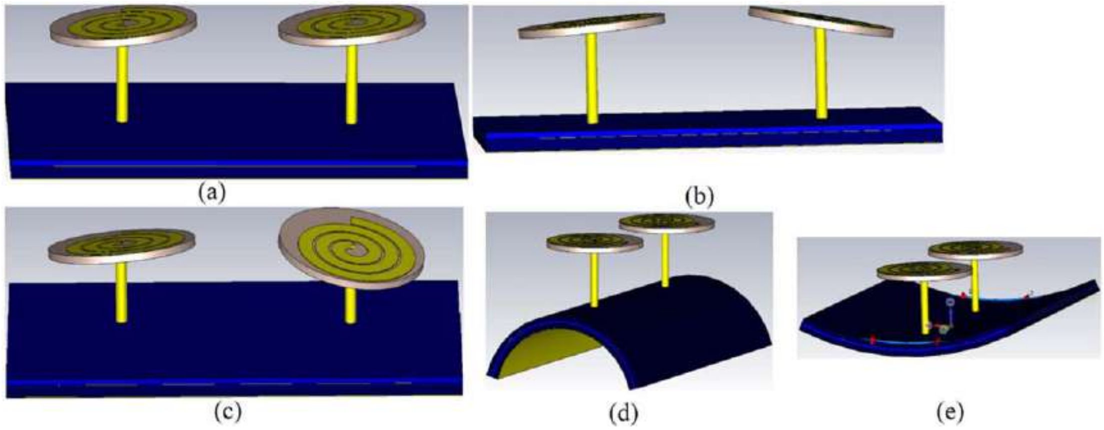

Figure 24. The flexibility evaluation setup towards the X and *Y* axis a: buttons tilted by X = 15°, b: both buttons tilted by X = 15° and X = −15°, c: both buttons tilted by Y = 15° and Y = −15°, d: LWA tilted by 15 0°, e: LWA tilted by 25°.

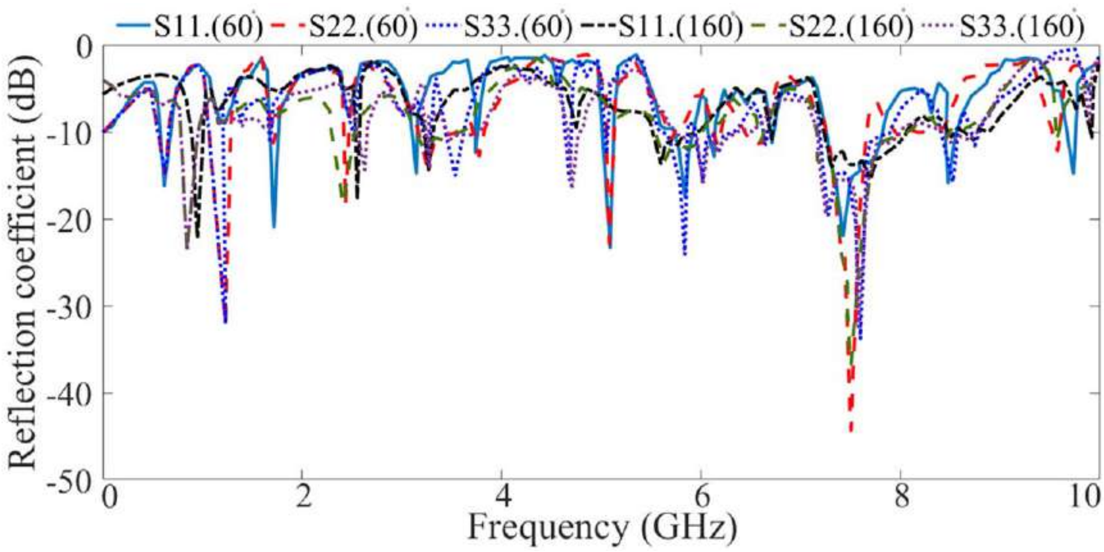

Figure 25. The antenna's reflection coefficient results in flexibility evaluation.

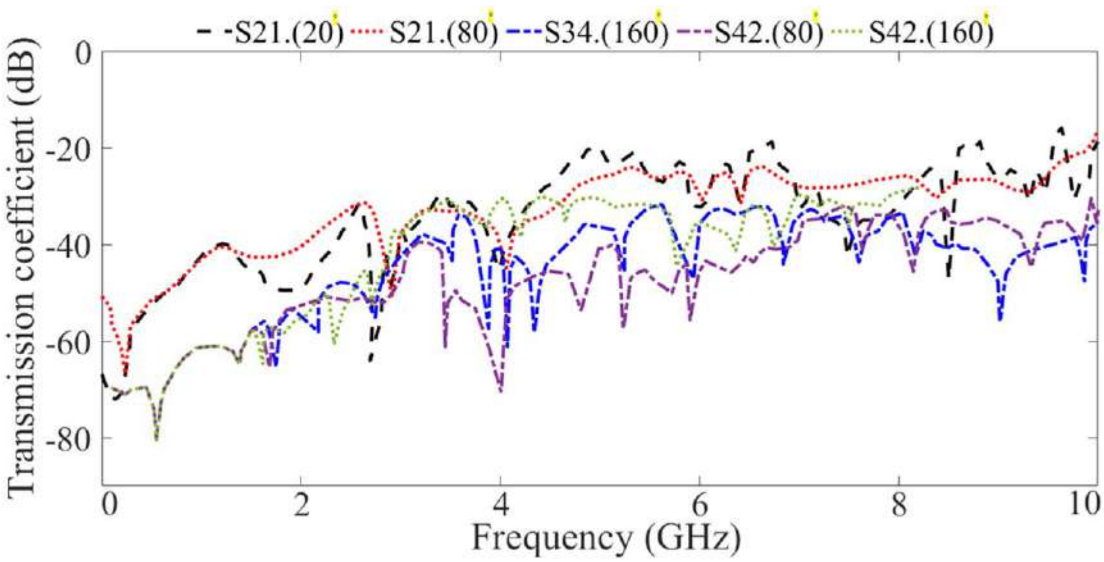

Figure 26. The antenna's transmission coefficient results in flexibility evaluation.

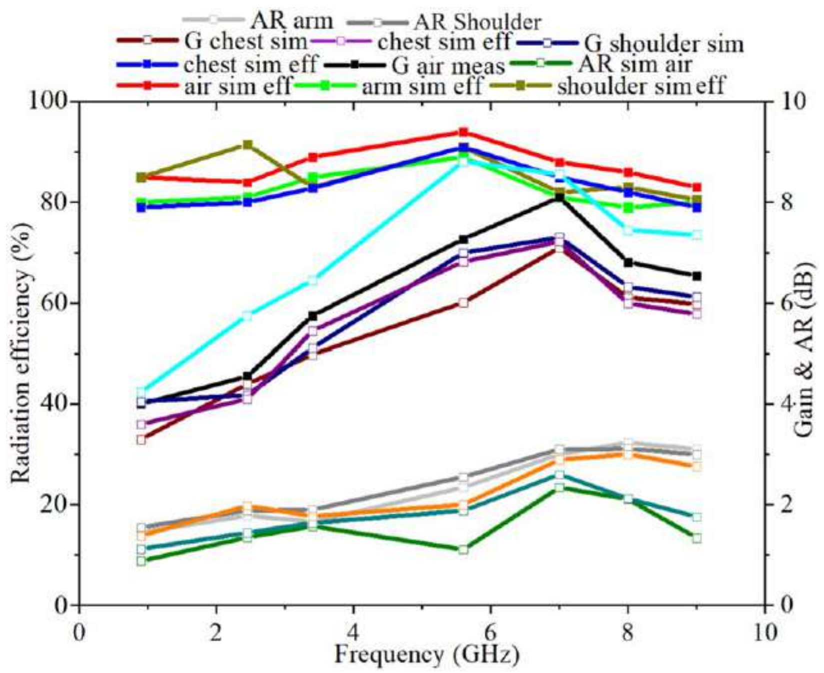

Figure 27. Gain, AR, and radiation efficiency results of MIMO antenna in air and on the body.

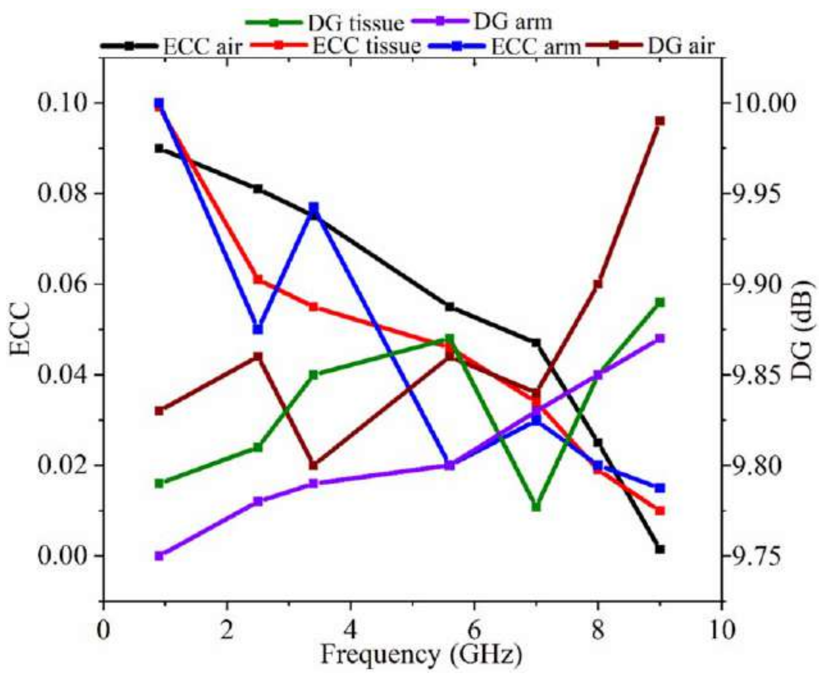

Figure 28. DG and ECC values of MIMO antenna in air and on the body.

Table 2 presents the antenna's experimental and simulated radiation properties in both on-body (arm, chest, and shoulder) and off-body configurations. A satisfactory correlation can be observed between the simulated and measured evaluations of the antenna. Additionally, the antenna exhibits a radiation efficiency of over 85% in both off-body and on-body versions across the entire bandwidth range. Regarding the on-body measurement, only measurements on the chest were performed. Table 2 also indicates that the gain variation at 7.2 GHz is at its maximum level on the chest, arm, and shoulder. Additionally, the simulated maximum gain is 8.5 dBi in air, reducing by almost 1.3 dBi when the antenna is on the body. It is clear that the gain level is lower on the chest compared to the gain on the arm and shoulder due to the thicker multiple-layer nature of the chest compared to the arm and shoulder.

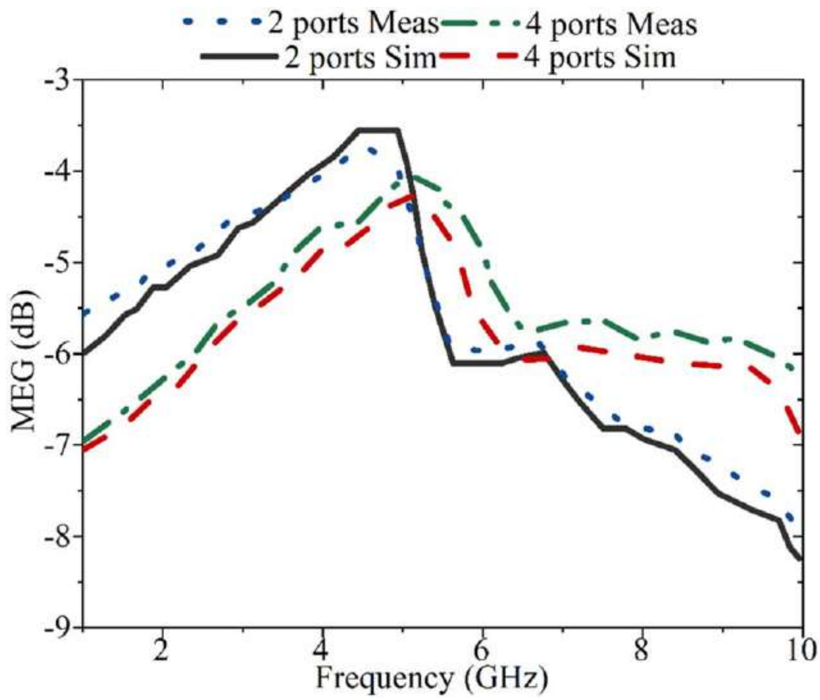

Figure 29. The measured and simulated MEG of the proposed antenna for both two and four ports.

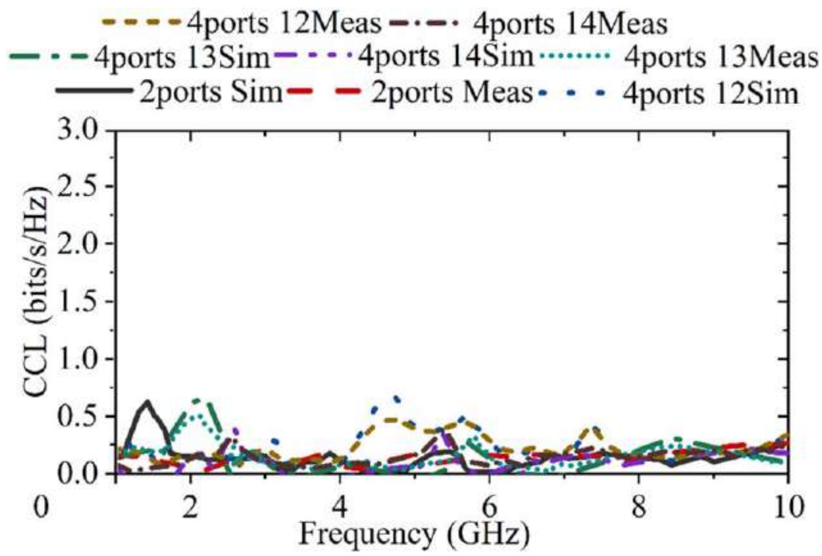

Figure 30. The measured and simulated CCL of the proposed antenna for both two and four ports.

The antenna's resistance to folding is evaluated after analyzing the SAR values to demonstrate its effectiveness on the human body with minimal SAR and impacts. We folded the antenna's button and LWA elements along the X and Y axes to assess their functionality when worn. It is to simulate the effects of actual wearable conditions on antenna performance. As depicted in figure 24, the antenna can be folded up to 30 degrees in both the X and Y directions at the button and up to 190 degrees at the LWA while maintaining proper functionality.

The bending of the proposed antenna's button component or LWA part is illustrated in figures 25 and 26 concerning the S-parameters. It demonstrates a slight shift in the antenna's reflection and transmission coefficients due to the folding. Consequently, several stopbands were created within the operational bandwidth after bending. However, the band still encompasses the crucial resonances for the intended applications, and the device continues to function successfully within those bands. These figures illustrate how the antenna's transmission and reflection coefficients shift after rotation. Figure 26 presents the transmission results in S21 and S31 for various angles (a-d), and the reflection coefficient results in S11 through S33 for similar angles (a-d).

Table 3. Comparison of the proposed fabric antenna with previously reported work on MIMO antennas.

Ref	Freq. (GHz) Off/On	Polarization	Max Eff (%)	Max Gain (dBi)	Size (mm) L × W @	DG (dB)	Ports/wearable	ECC	CCL (bits/s/Hz)	MEG (dB)	Isolation Techniques	Isolation (dB)
[15]	2.3, 2.5, 2.4, 3.4–3.6	N/A	70	5	$0.50\lambda_0 \times 0.65\lambda_0$ @2.5 GHz	N/A	3/no	<0.1	N/A	N/A	Radiator as isolation element	15
[18]	3.2–3.85, 5.15–5.35, 5.72–5.82	LP	93	N/A	$0.26\lambda_0 \times 0.23\lambda_0$	10	2/yes	<0.06	<0.2	N/A	Spacing	>26
[19]	3.18–4.60, 8.89–12	N/A	N/A	<6	$0.79\ \lambda_0 \times 0.79\ \lambda_0$ @3.8 GHz	N/A	4/yes	<0.2	<0.7	N/A	left–right extended Slotted ground stub	20.5
[20]	3.5–11	N/A	N/A	6	$0.63\ \lambda_0 \times 0.63\ \lambda_0$ @ 3.5 GHz	>9.9	4/yes	<0.01	<1.25	N/A	Orthogonal	>17
[21]	3.34–5.01, 8.9–9.2	N/A	N/A	N/A	$0.61\ \lambda_0 \times 0.61\ \lambda_0$ @3.34 GHz	N/A	4/yes	<0.17	N/A	N/A	interconnection between ground planes	>20
[22]	4.4–5	N/A	90	<4	$1.33\lambda_0 \times 1.03\ \lambda_0$ @4.5 GHz	N/A	4/yes	N/A	N/A	N/A	orthogonal arrangements	>17
[23]	3.1–12	Double	93	4.62	$0.52\ \lambda_0 \times 0.52\ \lambda_0$ @3.4 GHz	<9.9	4/yes	<0.08	<0.13	N/A	orthogonal arrangements	>17
[24]	2.74 to 4.41	N/A	N/A	<5	$0.86\ \lambda_0 \times 0.86\ \lambda_0$ @3.5 GHz	>9.6	4/yes	<0.2	N/A	±0.3	meander line structure	>19
[41]	2.40–2.48	CP	N/A	2.36	$0.67\ \lambda_g \times 0.67\lambda_g$ @3GHz	9.77	4/yes	<0.23	<0.1	N/A	orthogonal arrangements	>25
[42]	5–6.6	N/A	80	9.5	$0.88\ \lambda_0 \times 0.83\lambda_0$ @5.5 GHz	9.89	4/yes	N/A	N/A	N/A	EBG&MTS	>34
[43]	2.45	N/A	40	0.5	$0.23\ \lambda_0 \times 0.20\lambda_0$ @2.5 GHz	9.98	2/yes	0.025	<0.12	N/A	decoupling stub	<30
[44]	2.4–2.484, 3.2–3.85, 5.15–5.35, 5.72–5.825	N/A	93	N/A	$0.44\ \lambda_0 \times 0.28\ \lambda_0$ @3.4 GHz	<9.97	2/yes	<0.06	N/A	N/A	back-to-back E-shaped stub	N/A
[45]	2.2–3.5 4.8–6.2 7.8–9.8	N/A	<97	<6	$0.6\ \lambda_0 \times 0.6\ \lambda_0$ @5GHz	<10	4/yes	0.0001	<0.25	<−6	Spacing	<30
[46]	3–5	CP	>95	7.1	$0.75\ \lambda_0 \times 0.75\ \lambda_0$ @3.8 GHz	>9.9	4/no	<0.002	<11.23	N/A	diagonal slots and stub	<22
This work	0.86–2.75, 2.9–4.85, 5.75–6.15, 8–9.85	LP/CP	92.7	8.25	40 × 30	<10	4/Yes	<0.05	<0.3	<3.5	Neuralization network	<23

The antenna's diversity evaluation is demonstrated by exploring and analyzing factors in both on-body and off-body settings, as shown in figures 27–30. The diversity gain (DG) of almost ten dB and the envelope correlation coefficient (ECC) of less than 0.05 highlight the excellent diversity the suggested MIMO antenna provides. Moreover, the axial ratio (AR) remains below three at the resonances. It is important to note that the values of these parameters are likely to be consistent in both on-body and off-body scenarios. Additionally, the effects of these parameters were minimized when the antenna was close to the skin.

Two additional parameters should be evaluated for a MIMO antenna: MEG and CCL. Figures 29 and 30 present the variations of MEG and CCL, respectively, for the proposed MIMO antenna. MEG and CCL fall within acceptable ranges for the working bandwidth of the MIMO antenna. MEG represents the performance gain of an MIMO antenna while accounting for environmental effects. Figure 29 depicts the MEG analysis conducted for both 2-port and 4-port MIMO antennas. To ensure a well-designed 2-port MIMO antenna with the same input power level at ports, the MEG must be less than −3 dB. The same trend applies to 4-port MIMO antennas. CCL is the maximum acceptable value of channel loss that can be allowed for successful transmission over a communication channel. For reliable communication, the CCL should be less than 0.4 bits/s/Hz. CCL and MEG can be calculated using Equations (2–6) [39, 40] for two and 4-port MIMO antennas, respectively. Figure 30 shows the CCL value, significantly less than 0.25 bits/s/Hz at all working bands for the proposed 2-port and 4-port antennas. Lastly, table 3 compares the proposed work with recently developed three and four-port MIMO antennas designed for 5G and WBAN applications.

4. Conclusions

An innovative multi-band four-port MIMO antenna comprised two individual spiral button antennas and a leaky wave antenna (LWA). The spiral button antenna coupled with the complementary hexagonal split ring resonator (CHSRR) behind it as a ground offers a circular polarization. On the other hand, the LWA was fed using the aperture coupled technique with its coupled slot ground cut by three periodic elliptical slots and three nested circular SRR to broaden the bandwidth, enhance efficiency and gain, improve the circular polarization (CP), and reduced the dimensions. The LWA's patches were particularly cut by nested U-shape slots and then separated by a comb-shape neutralization network to tilt off the radiation towards the broadside and enhance the isolation, respectively. It also offers a maximum radiation efficiency and gain of less than 93% and 8.3 dBi, respectively. It also covers the frequency bands associated with WBANs application and 5G, sub-6 GHz, and X-band communications. The MIMO antenna exhibits an ECC of less than 0.05, a maximum DG of almost 10 dB, an axial ratio (AR) of less than 3, an MEG of less than −3 dB, less than 0.25 bits/s/Hz, and a maximum isolation of 22 dB, which makes it well-suited for MIMO applications with high diversity. The high-performance characteristics of the proposed antenna are simulated and then measured for both off-body and on-body applications on a voxel body. Folding and tilting analyses are also conducted to assess the antenna's adaptability. The antenna demonstrates strong agreement between the simulated and measured results. The proposed antenna will be a potential candidate as a solution for various communication challenges in laptop communications, the extended WLAN frequency range, and enabling improved coordination among soldiers and nurses on the ground.

Acknowledgments

The authors thank the Deanship of Scientific Research at ATU for funding this work under the Research Priorities.

Data availability statement

All data that support the findings of this study are included within the article (and any supplementary files).

ORCID iDs

Tale Saeidi https://orcid.org/0000-0002-0995-3364
Saeid Karamzadeh https://orcid.org/0000-0003-0669-0746

References

[1] Deng J-Y, Li J-Y and Guo L-X 2018 Decoupling of a Three-Port MIMO Antenna with Different Impedances Using Reactively Loaded Dummy Elements *IEEE Antennas Wirel. Propag. Lett.* **17** 430–3

[2] Yan S, Soh P J and Vandenbosch G A 2015 Compact All-textile Dualband Antenna Loaded with Metamaterial Inspired Structure *IEEE Antennas Wirel. Propag. Lett.* **14** 1486–9

[3] Singh S and Verma S 2022 Printed compact four-port wearable MIMO antennas for wideband wireless applications *Int. J. Microwave Wireless Technolog.* **15** 1–7
[4] Simorangkir R B V B, Yang Y, Matekovits L and Esselle K P 2016 Dual-Band Dual-Mode Textile Antenna on PDMS Substrate for Body-Centric Communications *IEEE Antennas Wirel. Propag. Lett.* **16** 677–80
[5] Ivsic B, Bonefacic D and Bartolic J 2013 Considerations on Embroidered Textile Antennas for Wearable Applications *IEEE Antennas Wirel. Propag. Lett.* **12** 1708–11
[6] Mahmood S N, Ishak A J, Saeidi T, Alsariera H, Alani S, Ismail A and Soh A C 2020 Recent advances in wearable antenna technologies: A review *Prog. Electromagn. Res. B* **89** 1–27
[7] Dang Q H, Chen S J, Ranasinghe D C and Fumeaux C 2021 A Frequency-Reconfigurable Wearable Textile Antenna with One-Octave Tuning Range *IEEE Trans. Antennas Propag.* **69** 8080–9
[8] Chen S J, Fumeaux C, Ranasinghe D C and Kaufmann T 2014 Paired Snap-On Buttons Connections for Balanced Antennas in Wearable Systems *IEEE Antennas Wirel. Propag. Lett.* **14** 1498–501
[9] Hu X, Yan S and Vandenbosch G A E 2018 Compact Circularly Polarized Wearable Button Antenna with Broadside Pattern for U-NII Worldwide Band Applications *IEEE Trans. Antennas Propag.* **67** 1341–5
[10] Hu X, Yan S, Zhang J, Volski V and Vandenbosch G A E 2021 Omni-Directional Circularly Polarized Button Antenna for 5 GHz WBAN Applications *IEEE Trans. Antennas Propag.* **69** 5054–9
[11] Zhang J, Meng J, Li W, Yan S and Vandenbosch G A E 2021 A Wearable Button Antenna Sensor for Dual-Mode Wireless Information and Power Transfer *Sensors* **21** 5678
[12] Elfergani I, Iqbal A, Zebiri C, Basir A, Rodriguez J, Sajedin M, Pereira A D O, Mshwat W, Abd-Alhameed R and Ullah S 2020 Low-Profile and Closely Spaced Four-Element MIMO Antenna for Wireless Body Area Networks *Electronics* **9** 258
[13] Iqbal A, Al-Hasan M, Ben Mabrouk I and Nedil M 2020 Compact SIW-Based Self-Quadruplexing Antenna for Wearable Transceivers *IEEE Antennas Wirel. Propag. Lett.* **20** 118–22
[14] Wang H, Liu L, Zhang Z, Li Y and Feng Z 2014 Ultra-Compact Three-Port MIMO Antenna with High Isolation and Directional Radiation Patterns *IEEE Antennas Wirel. Propag. Lett.* **13** 1545–8
[15] Chen W and Lin R 2020 Three-port MIMO antennas for laptop computers using an isolation element as a radiator *Int. J. RF Microw. Comput. Eng.* **31** 1–11e22326
[16] Mohanty A and Behera B R 2021 Design of a 3-Port Compact MIMO Antenna Based on Characteristics Mode Analysis Approach *Progress in Electromagnetics Research C* **111** 173–89
[17] Jaiswal R K, Kumari K, Sim C-Y-D and Srivastava K V 2021 Three-port circularly polarized MIMO antenna for WLAN application with pattern and polarization diversity *Microwave Opt. Technol. Lett.* **63** 1927–34
[18] Biswas A K and Chakraborty U 2019 Compact wearable MIMO antenna with improved port isolation for ultra-wideband applications *IET Microwaves, Antennas Propag* **13** 498–504
[19] Biswas A K, Biswas S, Haldar S and Nandi A 2024 A highly decoupled flexible 4-element MIMO antenna with band notched characteristics for ultra wide-band wearable applications *International Journal of Electronics and Communications* **173** 154985
[20] Ibrahim A A, Ahmed M I and Ahmed M F 2022 A systematic investigation of four ports MIMO antenna depending on flexible material for UWB networks *Sci. Rep.* **12** 14351
[21] Kulkarni N P, Bahadure N B, Patil P D and Kulkarni J S 2022 Flexible interconnected 4-port MIMO antenna for sub-6 GHz 5G and X band applications *AEU* **152** 154243
[22] Prithivirajana V, Poongodi S, Thandaiah Prabu R, Kamatchi S and Anand A 2023 A small conformal wearable four-port wideband antenna for 5G applications *International Journal of Electronics Letters* **19** 1–17 https://doi.org/10.1080/21681724.2023.2267205
[23] Govindan T, Palaniswamy S K, Kanagasabai M, Kumar S, Marey M and Mostafa H 2022 Design and Analysis of a Flexible Smart Apparel MIMO Antenna for Bio-Healthcare Applications *Micromachines* **13** 1919
[24] Roy S, Biswas A K, Ghosh S and Chakraborty U 2021 Isolation improvement of dual-/quad-element textile MIMO antenna for 5G application *J. Electromagn. Waves Appl.* **35** 1337–53
[25] Zhang J, Du C and Wang R 2022 Design of a Four-Port Flexible UWB-MIMO Antenna with High Isolation for Wearable and IoT Applications *Micromachines* **13** 2141
[26] Iqbal A, Nasir J, Qureshi M B, Khan A A, Rehman J U, Owais, Rahman H U, Fayyaz M A B and Nawaz R 2022 A CPW fed quad-port MIMO DRA for sub-6 GHz 5G applications *PLoS One* **17** e0268867
[27] Wu A, Zhao M, Zhang P and Zhang Z 2022 A Compact Four-Port MIMO Antenna for UWB Applications *Sensors* **22** 5788
[28] Ali S M, Jeoti V, Saeidi T and Wen W P 2019 Design of compact microstrip patch antenna for WBAN applications at ISM 2.4 GHz *Indonesian Journal of Electrical Engineering and Computer Science* **15** 1509–16
[29] Ali bakhshikenari M, Virdee B S, See C H, Abd-Alhameed R A, Falcone F and Limiti E 2019 High-Isolation Leaky-Wave Array Antenna Based on CRLH-Metamaterial Implemented on SIW with $\pm 30^{\circ}$ Frequency Beam-Scanning Capability at Millimetre-Waves *Electronics* **8** 642
[30] Gómez-Tornero J L, Quesada-Pereira F D and Álvarez-Melcón A 2005 Analysis and design of periodic leaky-wave antennas for the millimeter waveband in hybrid waveguide-planar technology *IEEE Trans. Antennas Propag.* **53** 2834 –42
[31] Nasimuddin N, Chen Z N and Qing X 2013 Substrate Integrated Metamaterial-Based Leaky-Wave Antenna with Improved Boresight Radiation Bandwidth *IEEE Trans. Antennas Propag.* **61** 3451–7
[32] Halilu Jabire A, Sani S, Saminu S, Adamu M J and Hussein M I 2022 A crossed-polarized four port MIMO antenna for UWB communication *Heliyon* **9** e12710
[33] Yuan H, Qu S, Zhang J, Zhou H, Wang J, Ma H and Xu Z Dual-Band Dual-Polarized Spiral Antenna for Chinese Compass Navigation Satellite System *Progress In Electromagnetics Research Letters* **46** 25–30
[34] Agastra E, Lucci L, Pelosi G and Selleri S 2012 High Gain Compact Strip and Slot UWB Sinuous Antennas *Int. J. Antennas Propag* **2012** 721412
[35] Mohamad S, Cahill R and Fusco V 2014 Selective High Impedance Surface Active Region Loading of Archimedean Spiral Antenna *IEEE Antennas Wirel. Propag. Lett.* **13** 810–3
[36] Rao P H, Sreenivasan M and Naragani L 2009 Dual Band Planar Spiral Feed Backed by a Stepped Ground Plane Cavity for Satellite Boresight Reference Antenna Applications *IEEE Trans. Antennas Propag.* **57** 3752 –6
[37] Bose S, Ramraj M and Raghavan S Design, analysis and verification of Hexagon Split Ring Resonator based Negative Index Metamaterial, 2012 Annual IEEE India Conference (INDICON), 28 January 2013
[38] Akkaya E and Güneş F 2021 Ultrawideband, high performance, cavity-backed Archimedean spiral antenna with Phelan balun for direction finding and radar warning receiver applications *Int. J. RF Microw. Comput. Eng.* **31** e22596

[39] Kaushal V, Birwal A and Patel K 2023 Diversity characteristics of four-element ring slot-based MIMO antenna for sub-6-GHz applications, *ETRI Journal* **45** 581–93

[40] Govindan T, Palaniswamy S K, Kanagasabai M, Rao T R, Nabi Alsath M G, Kumar S, Velan S, Marey M and Aggarwal A 2021 On the design and performance analysis of wristband MIMO/diversity antenna for smart wearable communication applications, *Sci. Rep.* **11** 21917

[41] Iqbal A, Smida A, Alazemi A J, Waly M I, Mallat N K and Kim S 2020 Wideband Circularly Polarized MIMO Antenna for High Data Wearable Biotelemetric Devices *IEEE Access* **8** 17935–44

[42] Althuwayb A A, Alibakhshikenari M, Virdee B S, Rashid N, Kaaniche K, Ben Atitallah A, Armghan A, Elhamrawy O I, See C H and Falcone F 2022 Metasurface-Inspired Flexible Wearable MIMO Antenna Array for Wireless Body Area Network Applications and Biomedical Telemetry Devices *IEEE Access* **11** 1039–56

[43] Gupta A, Kansal A and Chawla P 2020 Design of a wearable MIMO antenna deployed with an inverted U-shaped ground stub for diversity performance enhancement *Int. J. Microw. Wirel. Technol.* **13** 76–86

[44] Rekha S and Let G S 2022 Design and SAR Analysis of Wearable UWB MIMO Antenna with Enhanced Isolation Using a Parasitic Structure *Iran. J. Sci. Technol. Trans. Electr. Eng.* **46** 291–301

[45] Hussain M, Abbas Awan W, Alzaidi M S and Elkamchouch D H 2023 Self-decoupled tri-band MIMO antenna operating over ISM, WLAN, and C-band for 5G applications *Heliyon* **9** e17404

[46] Kartha M M and Jayakumar M 2023 Circularly polarized stub-loaded annular ring patch antenna for 2×2 MIMO satellite application *Measurement* **217** 113044